



University of Otago

Department of Physics

Dodd-Walls Centre for Photonic and Quantum Technologies

Direct Measurements of Collisional Dynamics in Ultracold Atom Triads

Luke Reynolds

A thesis submitted for the degree of

Master of Science in Physics

Supervisor: Dr. Mikkel Andersen

Submitted: June 29, 2018

Declaration

This thesis is an account of research undertaken between July 2017 and June 2018 at The Department of Physics, Division of Science, University of Otago, Dunedin, New Zealand under the supervision of Dr. Mikkel Andersen.

Except where acknowledged in the customary manner, the material presented in this thesis is, to the best of my knowledge, original and has not been submitted in whole or part for a degree in any university.

June 29, 2018

Luke Reynolds

Acknowledgement

I would like to thank Mikkel first and foremost for taking me into a very enjoyable research group, teaching me the importance of simplicity and wide consideration in complex systems, constantly supporting my efforts, and keeping a pleasant and enthusiastic disposition for the entirety of my studentship. I am grateful for the opportunity to come to a new country and achieve an experimental goal under fantastic supervision.

I extend a big thank you to Eyal not only for the tireless effort and help in the lab, but for the mental support and camaraderie as well. It was a pleasure being able to work independently knowing that I always had the backup of a friend and colleague, which I looked to many, many times. The endless conversations during long shifts in the lab helped to maintain my sanity and learn new perceptions of the world.

Thank you to Rhys for always being available to ask questions, bounce ideas off of, help work on the experiment, and indulge my hopelessly dumb sense of humor. It was really nice to have a peer and friend throughout this project.

I am very grateful to have shared a lab space with Shijie. Even though we had adjacent focuses, you never turned down an opportunity to field my questions, explain concepts, debug problems with the experiment, and exude nothing but kindness throughout the year.

I always appreciated the welcome distractions from Daniel, Josh, Matt, Jelena, Quinn, and all of the other students around the department.

My tenure at Otago was made extremely smooth and easy thanks to Brenda, Bev, and all the staff in the Physics Department.

Finally, I thank my parents and sisters for the enormous love and support they have given me whether I am in the same house or across the world.

Abstract

In this thesis, I present experimental methodology and results for direct measurements of ultracold few-atom collision dynamics, which allows quantum processes to be observed at the single event level. Three individual ^{85}Rb atoms are prepared in a specific quantum state and near-deterministically loaded into separate far-off resonance optical tweezers. The three trapping potentials are then merged, allowing the atoms to interact. By controlling the parameters of this interaction – duration and density of the atom triad – time-dependent atom loss from the trap due to two- and three-body inelastic collisions is observed. The loss rate from two-body collisions, K_2 , is found to show a dependence on the trap beam intensity, which suggests that off-resonant photoassociative processes play a significant role in the system. In addition, the three-body recombination event rate constant, K_3 , is extracted from these loss measurements. The determination of K_3 in this manner marks a novel experimental measurement, as previous investigations have deduced the rate constant only by observing atom loss from a many-body sample. The measured few-body value for K_3 shows consistency with its prediction from established theory illuminating a promising path for future experiments to take in the field of few-atom studies.

Preface

Following the submission of this thesis, I, along with my supervisor Dr. Mikkel Andersen and other research associates further developed the results and discussion seen here. This continued work yielded conclusions from this project which differ from those presented. For a more complete and valid treatment of the content in Chapter 6, see the following article:

L. A. Reynolds, E. Schwartz, U. Ebling, J. Brand, and M. F. Andersen. Direct measurements of collisional dynamics in cold atom triads. *To be published.*

Contents

List of Figures	viii
List of Tables	x
1 Introduction	1
1.1 Thesis Structure	3
1.2 Author Contribution	4
I Background	
2 Laser Cooling and Trapping	5
2.1 Laser Cooling	5
2.2 Magneto-Optical Trap	7
2.3 Polarization Gradient Cooling	9
2.3.1 Sisyphus Cooling	11
2.4 Far-Off Resonance Traps (FORTs)	12
2.4.1 Classical Oscillator Description	13
2.4.2 Multi-Level Atoms	15
2.5 Single Atom Preparation through Light-Assisted Collisions	17
2.5.1 Long-Range Atomic Potentials	18
2.5.2 Landau-Zener Transition	20
2.5.3 Repulsive Light-Assisted Collisions	21
3 Ultracold Few-Body Systems	23
3.1 Atomic Collisions	24
3.1.1 Asymptotic Analysis	24
3.1.2 Scattering Length and Phase Shift	27
3.2 Three-Body Interactions	29
3.2.1 Hyperspherical Coordinates	29

3.2.2	Adiabatic Representation	31
3.2.3	Three-Body Recombination	32
3.2.4	Theoretical Prediction of Three-Body Recombination Rate	36
3.3	Modeling Population Dynamics	37
3.3.1	Model of Loss from BEC	38
3.3.2	Direct Atom Triad Loss Model	39

II Experimental Apparatus and Methods

4	Experimental Apparatus	41
4.1	Fundamental Setup	41
4.1.1	Vacuum System	41
4.1.2	Magneto-Optical Trap	43
4.2	Detection System	45
4.2.1	Single Atom Imaging	46
4.2.2	Counting Single Photons	47
4.3	FORT Loading Sequence	49
5	Implementation and Characterization of Multiple FORTs	50
5.1	Generation of Multiple Traps	50
5.2	Mapping of Trap Positions	53
5.2.1	Static Trap Positions	53
5.2.2	Merging Potentials	55
5.3	Assessment of Single Atom Temperature	56
5.4	Preparation of Extreme Spin Polarized Atomic States	58
5.5	Measurement Methods of Few-Body Collisions	62
5.5.1	Experimental Sequence	63

III Results and Discussion

6	Results of Atomic Loss	65
6.1	Measurements of Three-Atom Collisions	65
6.1.1	Atom-Loss Rates	66
6.1.2	Atomic Density	68
6.2	Two-Body Dynamics	69
6.3	Discussion of Results	70
6.3.1	Comparison to Results from BEC Experiments	72

7 Conclusion	73
Appendix A Direct Atom Triad Loss Model Solutions	76
Bibliography	79

List of Figures

2.1 Schematic of magneto-optical trap	8
2.2 Drawing of polarization configuration utilized in polarization gradient cooling	10
2.3 Sisyphus cooling mechanism diagram	12
2.4 Induced energy level shifts from far-off resonant light	16
2.5 Flow chart of light-assisted collisions in a FORT	18
2.6 Diagram of one-dimensional light-assisted collisions	19
2.7 Schematic picture of the Landau-Zener avoided crossing description of light-assisted collisions	20
3.1 Relative position vectors in a three-body system	29
3.2 Physical representation of hyperangles θ and φ	31
3.3 Diagram of hyperradial effective potential curves	33
4.1 Vacuum system schematic	42
4.2 Annotated level diagram for the ^{85}Rb D2 line in the MOT stage	44
4.3 Imaging system schematic	45
4.4 Annotated level diagram for the ^{85}Rb D1 and D2 lines during single atom imaging	47
4.5 Example of a corrected calibration histogram from SPCM	48
4.6 FORT loading sequence	49
5.1 Schematic of RF electronics used to generate multiple FORTs	51
5.2 Schematic of RF electronics used to stabilize the optical power of the FORT beam(s)	52
5.3 Example picture of three separated ^{85}Rb atoms in confined in static traps as seen by the EMCCD camera	54
5.4 Diagram of trap 'pouring' in the merging process	56

5.5	Example of a plot used to determine atomic temperature via the release and recapture method	57
5.6	Diagram of optical pumping technique accumulating atoms in the $ F' = 2, m_F = -2\rangle$ state	60
5.7	(a) Raman spectroscopy used in the testing of optical pumping efficiency (b) Rabi oscillations in population transfer from stimulated Raman transitions	61
5.8	Measurements of rates to calculate the efficiency of optical pumping. (a) Pump-in time (b) Pump-out time	62
5.9	Schematic timeline of three-body collision experiment	63
6.1	Plots of trap population versus wait time at varying 'deep' trap levels .	67
6.2	A general schematic representation photoassociation due to off-resonant coupling light	70

List of Tables

6.1 Three-body loss rates from experiment, γ_3 , with corresponding density and three-body loss event rate constant, K_3^{exp} , according to FORT potential depth	68
6.2 Comparison of three-body loss rates from experiment, γ_3 , to two-body loss rates, γ_2 , and two-body loss event rate constant, K_2^{exp} , according to FORT potential depth	69

1 | Introduction

The emergence of quantum mechanics throughout the past century in theory and experiment has allowed us to improve our understanding of nature in the microscopic realm at an incredible rate. Over the past few decades in particular, finer scales of observation came to light due to advances in techniques that probe atomic samples directly. Experimental progress in the field of atomic physics has generally come in the form of inferences from measurements made using an ensemble of atoms. Such averaging tends to hide effects that may only be visible on the single event level. Then if our goal is to thoroughly understand nature by stitching together the macroscopic and microscopic perspectives, we are led to an experimental setting of individual microscopic event observation.

Armed with knowledge of atom-light interactions stemming from as early as the 1900s, fundamental research in quantum manipulation has really excelled over the past few decades. Notably, two paths that this research follows are in the form of Bose-Einstein condensation (BEC) and single atom trapping. Surprisingly, Bose and Einstein predicted that a group of noninteracting bosons cooled below a certain level will largely coalesce into the lowest energy quantum mechanical ground state [1, 2]. That level is such that their de Broglie wavelength is greater than the mean spacing between particles. Famously, this theory became reality only in 1995 [3]. Since then, the BEC consistently proves its value as a platform to observe interesting quantum phenomena such as the formation of soliton trains and vortex rings [4], macroscopic quantum tunneling [5], and the well known "bosonova" experiment [6]. Furthermore, a substantial part of research in this field was, and still is, dedicated to observing unwanted loss mechanisms due to ultracold atomic collisions [7, 8]. These few-body processes manifest themselves in such many-body experiments as a detriment to BEC lifetimes and stability, and thus it is of great utility to understand few-body collisions in this regime.

Although undesirable at first, processes like three-body recombination, where two atoms bind to form a diatomic molecule, or dimer, while a third carries away excess energy and momentum, gained their own focus because of the realization that the governing physics is linked to the counterintuitive quantum phenomenon called the Efimov effect [9, 10]. Since it is not only interesting in its own right, but also perhaps the most important loss mechanism in trapped ultracold atoms, three-body recombination demands a more thorough investigation. If one has sufficient information regarding the atomic interactions at hand, the recombination rate may be calculated using the three-body Schrödinger equation. The interactions between atoms in most experimental settings though, tend to be quite complex and do not lend enough accuracy to be calculated. Further information about the dynamics of ultracold few-body systems must then be gained from direct experiment.

Few-atom observations became a reality first in 1979 with the successful confinement of a barium ion in a radio frequency electric field trap [11]. Contrary to ions, neutral atoms, which lack the readily available strong Coulombic interactions of ions, were not isolated until 1994 with confinement of a single neutral Cesium atom [12]. Since then, control over individual atoms or small sets of individual atoms has improved substantially. For example, utilizing the superfluid to Mott-insulator transition in BEC can be an efficient way of preparing single atoms in lattice sites [13, 14, 15] as well as using Penning ionization [16]. Both of these methods along with others employ an important tool referred to as a far-off resonant trap (FORT) [17]. A FORT provides a conservative non-dissipative potential with a long coherence time and the ability to control atomic interactions at a long and short range all while being nearly perfectly isolated from its external environment. Because of their efficacy and relative simplicity, FORTs are now widely used in neutral atom confinement.

When a sample of cold atoms is prepared to be loaded into a FORT, inducing light-assisted collisions serves as a generator of sub-Poissonian atom loading. The dynamics of the atoms in the cloud can be described as a collection of two-body interactions. If one of the atoms happens to undergo a transition to its electronically excited state due to the near-resonant light it is exposed to, then the preceding atom-atom interaction properties are changed. Depending on the detuning from resonance of the interaction inducing light, the atoms are transferred to either an attractive (red-detuned) or repulsive (blue-detuned) potential. This potential curve then determines resultant energies of the atoms after their collision. Initially, this technique sought to allow only one atom into a pair of tight optical tweezers with loading efficiencies of about 50% depending on if the number of atoms in the original sample was even

or odd when using red-detuned collision light [18, 19]. Alternatively, when inducing repulsive light-assisted collisions from blue-detuned light, near-deterministic single atom loading efficiency up to 91% results [20, 21].

In this thesis, I report direct measurements of three-body recombination from a single event scale. By using repulsive light assisted collisions, single atom loading in all three separate microtraps is achieved in 35.7% of experiment realizations. Then the traps are adiabatically swept to merge to potential barriers and form one FORT containing three atoms prepared in the same hyperfine state, $|F = 2, m_F = -2\rangle$. By varying the depth of this potential well and the time in which the atoms are allowed to interact, time-dependent trap loss is observed. This loss rate corresponds to a three-body recombination rate coefficient of $\overline{K_3^{exp}} = (7.65 \pm 0.47) \times 10^{-25} \text{ cm}^6/\text{sec}$, which compared to the prevailing theoretical model yielding $K_3^{th} = (7.47 \pm 0.51) \times 10^{-25} \text{ cm}^6/\text{sec}$, shows good mean agreement.

1.1 Thesis Structure

This thesis is organized into three main parts. Part I, which includes Chapters 2 and 3, is a review of the established theory behind relevant topics in laser cooling, trapping, and manipulation of ultracold few-body systems. **Chapter 2** describes the requirements of cooling and containing a cloud of neutral atoms in a magneto-optical trap (MOT), the principles of the widely used experimental tool optical tweezers, as well as methods of cooling atoms beyond their Doppler limit. This chapter also discusses light-assisted collisions between cold atoms in order to efficiently prepare a single atom sample. **Chapter 3** highlights the theoretical motivation of this experiment; directly observing three-body recombination in a few-body system. It includes a description of the general theory of atomic collisions followed by a more in-depth look at three-body interactions. The chapter concludes with the model of population decay within the trap used in the experimental sections.

Part II begins with **Chapter 4**, which details the experimental setup employed in throughout thesis including laser systems, vacuum chamber platform, imaging techniques, and computer based control scheme. This chapter also explains how each of these pieces are utilized in the near-deterministic preparation of a single ^{85}Rb atom. **Chapter 5** catalogs the adaptations made to the already present experimental apparatus in order to accommodate the loading of single atoms into three separate microtraps. This includes a schematic of the system of RF electronics used to input

multiple driving frequencies to an acousto-optic modulator (AOM) and adiabatically merge the three traps into one by sweeping these frequencies. The details necessary for potential repetition of this method, e.g. required trap separation, are also given in this portion. Finally, it lists the extension of the experimental sequence in Chapter 4 made to produce the results in Part III.

In this experiment, I investigate the population dynamics of three identical bosons confined in a FORT. All three atoms may collide and escape the trap in a process referred to as three-body recombination, and the three-body perspective of the experimental results is presented and discussed in **Chapter 6**. There are also processes of two-body loss and one-body loss through heating from off-resonant scattering possible in our experiment. This necessitates a further analysis into these potential outcomes of our experiment, which are also presented in Chapter 6. Finally, I relate the resulting rate coefficients to those obtained from experiments in Bose-Einstein condensation within a final discussion of experimental results.

1.2 Author Contribution

I, along with a set of present and past colleagues carried out the experimental work discussed in this thesis. The initiation and conceptualization of the experiment at large was done by the group's principal investigator, Dr. Mikkel Andersen. In specific, the experimental apparatus detailed in Chapter 4 as well as the main sequence listed there can be attributed to a collaboration of former PhD students and postdoctoral fellows: Dr. Andrew Hilliard, Matt McGovern, Dr. Alicia Carpentier, Dr. Pimonpan Sompet, Yin Hsien Fung, and Dr. Eyal Schwartz. Beginning in Chapter 5, additions to the existing experiment were made by myself and postdoctoral fellow Dr. Eyal Schwartz to adapt the system for multiple trap functionality. All following results in Part III were collected using the adapted experimental setup and mathematically analyzed by myself under the supervision of Dr. Eyal Schwartz.

2 | Laser Cooling and Trapping

At the base level of importance to the experiment listed in the thesis lies laser cooling and confinement of neutral atoms in a magneto-optical trap (MOT) and far-off resonance trap (FORT). In the first section of this chapter I will outline the theory of laser cooling and trapping techniques utilized in the later discussed experiment. I detail Doppler cooling and containment of atoms in a MOT, cooling past the Doppler limit using polarization gradient cooling (PGC), then their loading into a FORT. This will also include a discussion of the effect of the FORT light on the structure of the atoms. Finally, I detail the theory of light-assisted collisions that serves to isolate a single atom in the trap through inelastic collisions.

2.1 Laser Cooling

When light is irradiated on matter it exerts a force called radiation pressure. This is because light is made up of photons that each carry a momentum given by [22]

$$p = \frac{h}{\lambda} = \hbar k \quad (2.1)$$

where the wave vector $k = \frac{2\pi}{\lambda}$. Typically, a discussion of atomic absorption of a photon will describe the excitation of the electron due to the energy of the photon and the acceptance of the photon's angular momentum by the atom based on its angular momentum quantum number and various selection rules. The *linear* momentum of the photon is often left out of conversation because it is generally negligible. From simple conservation of momentum, an atom that absorbs a photon must feel some sort of recoil. The change in velocity of the atom, or recoil velocity, is given by,

$$\Delta v = \frac{\hbar k}{m} \quad (2.2)$$

for an atom of mass m . This means that many instances of imparted recoil serve to substantially change an atom's linear momentum, or slow it. Considering a two-level atom, it must emit the absorbed photon before it can absorb another. A cycle of absorption and spontaneous emission, which at minimum is twice the atomic lifetime, τ , is called scattering, and its accompanying force is called the scattering force, $\mathbf{F} = \frac{\hbar\mathbf{k}}{\tau}$.

Two aspects should be noted about the scattering force: it is not conservative because spontaneous emission is irreversible, and it is velocity dependent. The non-conservative nature of this force allows for cooling, or changing the spread of the atom cloud's velocity distribution, not just slowing individual atoms. The velocity dependence of the force complicates the cooling process because of the Doppler shift.

Consider an atom traveling toward the source of the light, say the $-x$ direction with some magnitude of velocity, v - so $\mathbf{v} = -\hat{x}v$. Now, if the laser beam of frequency ω traveling in the $+x$ direction is red-detuned, $\omega < \omega_0$ where ω_0 is the energy difference between atomic energy levels, then the frequency observed by the atom is given by,

$$\omega_{obs} = \left(1 - \frac{v}{c}\right) \omega \quad (2.3)$$

Thus, the laser is only resonant with a selected velocity group of the entire atomic sample. By adding a counterpropagating beam in the $-x$ direction, the velocity group selection becomes symmetric. Furthermore, this idea is easily extended to three dimensions by adding two more sets of counterpropagating beams in the y and z directions. This configuration is referred to as optical molasses and provides detuning selective cooling in each direction.

Doppler cooling in this manner does reach a defined limit. Spontaneous emission of photons causes heating of the atom, which competes with the cooling process. The two reach equilibrium at a point called the Doppler temperature, T_d ,

$$T_d = \frac{\hbar\Gamma}{2k_B} \quad (2.4)$$

where Γ is the natural linewidth of the atom and k_B is Boltzmann's constant. That means the Doppler cooling is limited by the properties of the particular atomic transition being addressed. As a pertinent example, the D_2 line in ^{85}Rb has a natural linewidth of $2\pi \times 6.07\text{MHz}$ [23], which sets the Doppler temperature at $146\mu\text{K}$.

2.2 Magneto-Optical Trap

As mentioned in the previous chapter, the scattering force is not conservative, which means that it can cool atoms but not confine them. If atoms are within optical molasses beams, they will eventually move out of them through diffusion. To trap atoms means there is a controllable potential well such that an atom moving toward the well's walls exchanges kinetic for potential energy. With the addition of magnetic fields placed in a specific geometry then, a magnetic trap forms due to the fact that a magnetic moment experiences a force within a magnetic field gradient. The combination of an optical molasses configuration of laser beams and a magnetic field trap, or magneto-optical trap (MOT), was first demonstrated as an effective atom confinement apparatus in 1985 [24], and proves to be an invaluable tool in cold atom experiments today.

In general, the potential energy of interaction between an atom with some nonzero magnetic moment, μ , with an inhomogeneous magnetic field, $\mathbf{B}(\mathbf{r})$, is,

$$V_{mag} = -\mu \cdot \mathbf{B}(\mathbf{r}) \quad (2.5)$$

The magnetic sublevels of the atom with corresponding quantum numbers, m_j , for some nonzero angular momentum, J , are shifted by the Zeeman energy, $E_Z = m_j g_j \mu_B B$, where g_j is the Landé g-factor and μ_B is the Bohr magneton. In an example two level atom, consider the angular momentum quantum numbers $J = 0$ for the ground state and $J' = 1$ for the excited state. This means that the excited state has a manifold of nondegenerate states given by $m'_j = 0, \pm 1$ each shifted in energy according to their m'_j value. Moreover, the split levels can only be accessed by light of a particular polarization: linear polarization for $m'_j = 0$ and circular polarization for $m'_j = \pm 1$. When a quantization axis is defined for the atoms, linearly polarized light along this axis is specified as π polarized and addresses transitions with $\Delta m_j = 0$. In addition, right or left circularly polarized light is specified as σ_{\pm} polarized respectively and addresses transitions with $\Delta m_j = \pm 1$.

With the combination of an inhomogeneous magnetic field and polarization-dependent momentum kicks, a restoring force emerges and favors the center of the trap. Consider a beam red-detuned from resonance incident on the above mentioned two-level atom that is σ_+ polarized from the $-x$ direction. This is accompanied by a counterpropagating red-detuned beam of σ_- polarization. In one dimension, the magnetic field then needs to be a linear gradient, $B = \frac{dB}{dx}x$. Now, when the atom

drifts spatially in the $-x$ direction, it has a high probability of scattering photons from the σ_+ polarized beam because the red-detuned light becomes closer to resonance with the Zeeman shifted energy levels, as seen in Fig. 2.1 [22]. Again, this delivers a scattering force in the direction of beam propagation. The same is true in the reverse case. Thus, the atom experiences an equilibrium state in the center of the one-dimensional trap. Of course, this idea is easily extended to three dimensions with three sets of counterpropagating beams (known as optical molasses configuration) and a quadrupole magnetic field. A convenient supplier of this magnetic field comes from coils set in an anti-Helmholtz configuration. This typical MOT scheme is represented in Fig. 2.1.

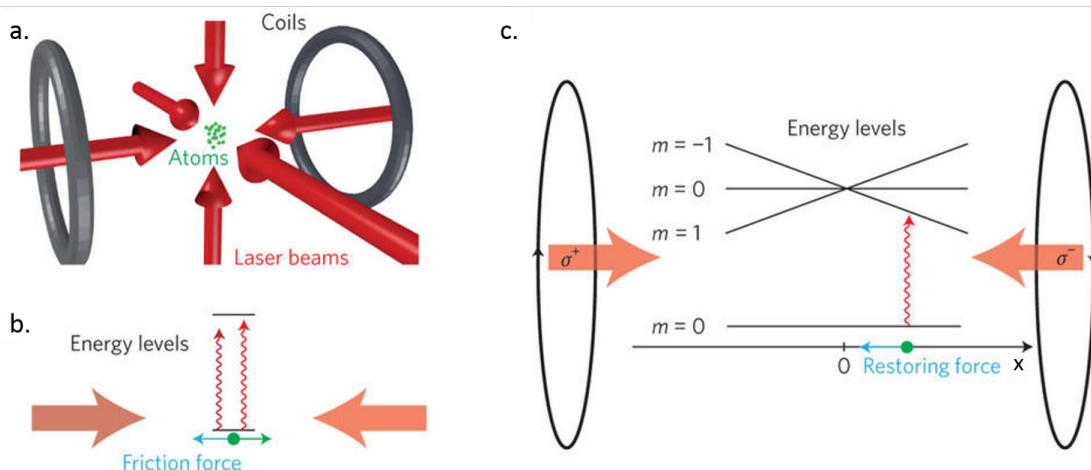


Figure 2.1: Magneto-optical trap: **a.** Spatial configuration of optical molasses beams and magnetic field coils. **b.** Linear restoring force (or 'friction' force) arises from position-dependent photon scattering. **c.** Complete MOT schematic accentuating the removal of sublevel degeneracy due to an applied magnetic field. This causes the position-dependent restoring force in **b**.

The choice of which atomic transition to apply this method is critical, as it needs to act in a similar manner the two-level atom. Namely, it needs to be a closed cyclic transition. In the case of ^{85}Rb , the $5\text{S}_{1/2}, F=3 \longrightarrow 5\text{P}_{3/2}, F=4$ transition is acceptable even though it is not truly closed. Since the excitation beam is red-detuned from the resonant frequency, there is a small probability that a transition to the $5\text{P}_{3/2}, F=3$ state will instead occur. It is then allowed to decay either back to the $F=3$ state and continue its cyclic transitioning or to the lower $F=2$ state, which will not be addressed by the incident light. This requires the use of a "repump" beam that is tuned to the $5\text{S}_{1/2}, F=2 \longrightarrow 5\text{P}_{3/2}, F=3$ transition and immediately deplete any population of atoms not resonant with the main transition light, referred to as "dark" state atoms.

2.3 Polarization Gradient Cooling

Until the late 1980s, the previously described Doppler limit was thought to be the minimum attainable atomic temperature. However, Lett et. al. successfully reported sodium atoms that were laser cooled approximately six times below the theoretical limit in 1988 [25]. This new phenomenon was quickly explored further [26] and theoretically detailed [27]. Because the laser beams used in laser cooling schemes are counterpropagating, interference occurs along the beam paths resulting in a spatially dependent polarization experienced by the atom. This polarization gradient works together with the multi-level complexity of the atom to provide an additional cooling mechanism referred to as polarization gradient cooling.

For explanatory convenience, consider the polarization gradient in one dimension with one set of the counterpropagating MOT beams, say along the z axis, described in the previous section. With the electromagnetic radiation assumed to be plane waves, the electric field along the z axis is written as,

$$\begin{aligned}\mathbf{E}^+(z, t) &= E_0^+ \cos(kz - \omega t) \hat{\epsilon} \\ &= E_0^+ (e^{i(kz-\omega t)} + e^{-i(kz-\omega t)}) \hat{\epsilon} \\ \mathbf{E}^-(z, t) &= E_0^- \cos(-kz - \omega t) \hat{\epsilon}' \\ &= E_0^- (e^{i(-kz-\omega t)} + e^{-i(-kz-\omega t)}) \hat{\epsilon}'\end{aligned}\tag{2.6}$$

where E_0^\pm represents the wave amplitude in the $\pm z$ direction, and $\hat{\epsilon}$ represents the polarization vector. The full field reads,

$$\begin{aligned}\mathbf{E}(z, t) &= \mathbf{E}^+(z, t) + \mathbf{E}^-(z, t) \\ &= \varepsilon^+(z) e^{-i\omega t} + \varepsilon^-(z) e^{i\omega t}\end{aligned}\tag{2.7}$$

Eq. 2.7 is separated as such to emphasize the spatial frequency components, $\varepsilon^\pm(z)$. Explicitly,

$$\varepsilon^+(z) = E_0^+ e^{ikz} \hat{\epsilon} + E_0^- e^{-ikz} \hat{\epsilon}'\tag{2.8}$$

The general polarization vectors are now specified for σ^\pm varieties,

$$\begin{aligned}\hat{\epsilon} &= \hat{\epsilon}_+ = -\frac{1}{\sqrt{2}}(\hat{\epsilon}_x + i\hat{\epsilon}_y) \\ \hat{\epsilon}' &= \hat{\epsilon}_- = \frac{1}{\sqrt{2}}(\hat{\epsilon}_x - i\hat{\epsilon}_y)\end{aligned}\tag{2.9}$$

Finally, inserting Eq. 2.9 into Eq. 2.8,

$$\epsilon^+(z) = \frac{1}{\sqrt{2}}(E_0^- - E_0^+) \epsilon_X - \frac{i}{\sqrt{2}}(E_0^- + E_0^+) \epsilon_Y \quad (2.10)$$

where,

$$\epsilon_X = \hat{\epsilon}_x \cos(kz) - \hat{\epsilon}_y \sin(kz) \quad (2.11)$$

$$\epsilon_Y = \hat{\epsilon}_x \sin(kz) + \hat{\epsilon}_y \cos(kz) \quad (2.12)$$

Qualitatively, Eq. 2.10 represents the resultant field from the superposition of two fields polarized along the ϵ_X and ϵ_Y axes rotating around the z axis with constant ellipticity, $\frac{(E_0^- - E_0^+)}{(E_0^- + E_0^+)}$. The simplifying assumption is that each arm of the counterpropagating beam has equal amplitude, $E_0^- = E_0^+$, which is very close to the experimental truth. In this case, the resultant field is *linearly* polarized along the ϵ_Y axis, which itself rotates along the z axis. Simply, at any stationary point along the z axis, the polarization felt by the atom is linear. Fig. 2.2 depicts the helical pattern of linear polarization development.

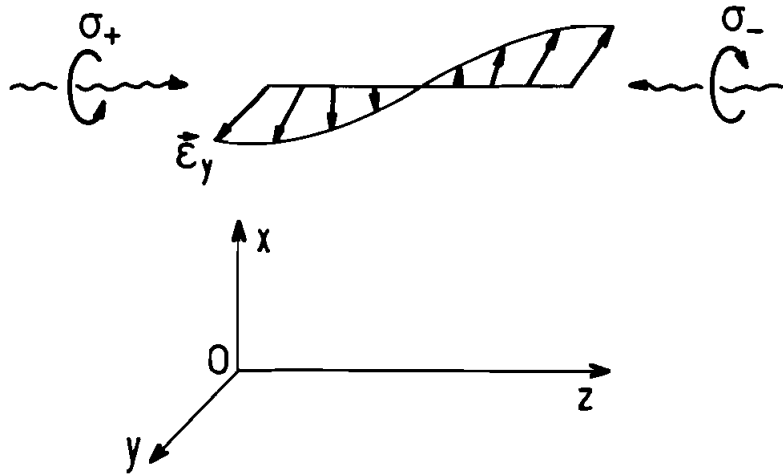


Figure 2.2: Two counterpropagating beams of opposite circular polarizations create a resultant linear polarization vector which rotates helically around the axis of beam propagation. [27]

Now that the polarization configuration is established, the actual cooling mechanism will be uncovered. When an atom within the counterpropagating beams moves along the same axis, a velocity-dependent atomic orientation develops [27]. Again, in the atom's rest frame, it sees the linear polarization rotating around the z axis at an angle, $\phi = -kz = -kvt$ when moving with velocity, v . Then consider a reference

frame that rotates with the polarization, such that it keeps a fixed direction. In this new frame, a fictitious magnetic field becomes apparent that is parallel to the rotation axis with amplitude proportional to the velocity. In addition, new non-adiabatic couplings between m_j ground states are introduced that are also proportional to the velocity leading to different steady state populations occupying them [27].

In other words, the photons from each beam are absorbed with different efficiencies. For example, in ^{85}Rb , atoms traveling toward the σ_+ beam will experience greater populations in the positive m_j states than in the negative. Furthermore, according to relative transition strengths, these atoms are much more likely to scatter photons from the σ_+ beam than the σ_- beam. This motion induced mechanism that forces population differences in the ground state sublevels of the atom consequently creates unequal radiation pressures from the two beams. The unbalance in radiation pressure applies a net friction force to the atom, decreasing its momentum and cooling it further below the Doppler limit. This new cooling mechanism is only relevant for atomic velocities much lower than in the realm of Doppler cooling [27].

2.3.1 Sisyphus Cooling

In the MOT system, there are three sets of retroreflected beams each in the σ_{+-} configuration. It would be a natural extension from the one dimensional case of PGC described in the above section to suggest that the same mechanism simply occurs in three dimensions. However, it is more complicated due to the introduced interference between the linearly polarization vectors (ϵ_Y). In addition, because the retroreflection of the three beams forms standing waves, intensity gradients arise in each beam path. Both of these consequences lead to an additional cooling mechanism called Sisyphus cooling [28].

For a description of this cooling process, consider a two-level atom with dressed states labeled $|1, n\rangle$ and $|2, n\rangle$ where n represents the interacting laser photons [29]. The bare states (not in the presence of a light field) are labeled by $|g\rangle$ for the ground state and $|e\rangle$ for the excited state. In the experimental situation, these correspond to the $F = 2$ hyperfine ground state ($5\ ^2\text{S}_{1/2}$) and $F' = 3$ excited state of the D1 line ($5\ ^2\text{P}_{1/2}$). When there is any atomic motion within the standing wave, the dressed levels depend on the local light intensity, which means they spatially vary. Importantly for consequences of cooling, the center-of-mass kinetic energy varies with the dressed state energies.

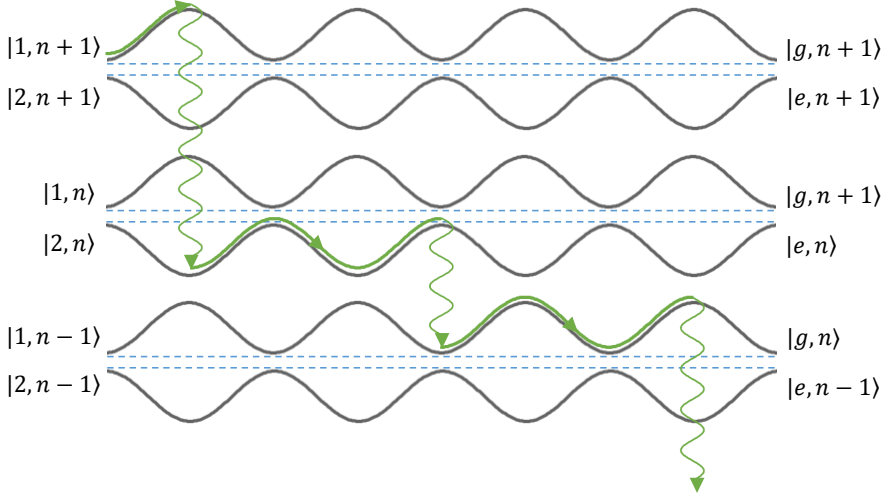


Figure 2.3: Graphical representation of the Sisyphus cooling mechanism in one-dimension. The black curves represent the dressed state energy levels with state labels on the left side. The blue dashed lines represent bare state energy levels.

As seen in Fig. 2.3, spontaneous emission between dressed states $1 \rightarrow 2$ occurs preferentially at the antinodes of the formed standing wave; this is also where the kinetic energy is minimum. The enhanced probability at these points owes to fact that the contamination of $|1, n+1\rangle$ by $|e, n+1\rangle$ and $|2, n\rangle$ by $|g, n\rangle$ is largest [29]. The reverse is true for transitions $2 \rightarrow 1$, as in the highest probability occurs at the nodal positions because their dressed energy maxima correspond to standing wave nodes. This repeating pattern of standing wave dependent dressed state transitions occurs decreasing the atom's kinetic energy on average because it is predominantly 'climbing' potential hills. Its thermodynamic equilibrium point, or cooling limit, is proportional to the amplitude of the standing wave variation [28]. In addition, cooling may only be realized in the case of a blue-detuned light field. When in the presence of a red-detuned light field, the dressed state transition probabilities are highest at points corresponding to potential energy troughs rather than peaks leading to an increase of atomic kinetic energy, or 'Doppler heating.'

2.4 Far-Off Resonance Traps (FORTs)

The confinement possibility of the MOT discussed previously is proficient for collecting groups of atoms on the order of 10^7 , but achieving isolation of single atoms requires a tighter and more controllable trap. Also, because MOT light must be tuned close to atomic resonance, excited state trap loss becomes significant. The optical

dipole force serves nicely as a further trapping mechanism because it is conservative, arising from the interaction between the neutral atom's induced dipole moment and the intensity gradient of the incident far-off resonant light field, and can create arbitrary shaped potential minima. Other key advantages of using a far-off resonance trap (FORT) are that high atomic densities are readily achievable ($\sim 10^{12} \text{ cm}^{-3}$) and a well-defined quantization axis [30]. Letokhov first considered utilizing the nodes or antinodes of an off-resonant standing wave as a one-dimensional confinement [31], and the experimental realization came in 1986 with Chu et. al. first optically trapping neutral atoms [32]. First, the optical dipole potential will be described classically in terms of an atom modeled as a simple oscillator subject to a classical radiation field. This explanation will then be formulated in a quantum picture of multi-level atoms. This approach mainly follows that of Grimm et. al. [17].

2.4.1 Classical Oscillator Description

The standard view of a neutral atom exposed to an electric field, \mathbf{E} , such as sitting in a laser beam, is that it develops an induced dipole moment, \mathbf{p} oscillating at a driving frequency, ω . Classically, this is as if the valence electron(s) is bound to the nucleus by some sort of spring. The expressions for these are written as [17],

$$\mathbf{E}(\mathbf{r}, t) = \hat{\epsilon} \tilde{E}(\mathbf{r}) e^{-i\omega t} + c.c. \quad (2.13)$$

$$\mathbf{p}(\mathbf{r}, t) = \hat{\epsilon} \tilde{p}(\mathbf{r}) e^{-i\omega t} + c.c. \quad (2.14)$$

where $\hat{\epsilon}$ represents the unit polarization vector, \tilde{E} the electric field amplitude, and \tilde{p} the dipole moment amplitude. These amplitudes are related simply by,

$$\tilde{p} = \alpha \tilde{E} \quad (2.15)$$

with α representing the complex polarizability of the atom meaning that the electric field may be out of phase with the induced dipole moment.

In order for the electric field to induce the dipole in the first place, it had to do work. Analogous to stretching the spring that the electron is attached to, that amount of work is $W = \frac{1}{2}kd^2$ where d is the dipole size, $\tilde{p} = ed$, and the 'spring constant' is $k = e\tilde{E}/d$. Then the amount of work can be rewritten as $\frac{1}{2}\mathbf{p} \cdot \mathbf{E}$. In general, the total energy of a dipole in an electric field is $U = -\mathbf{p} \cdot \mathbf{E}$. Then the interaction potential

from the induced dipole is [17],

$$U_{dip} = W + U = -\frac{1}{2}\langle \mathbf{p} \cdot \mathbf{E} \rangle = -\frac{1}{2\epsilon_0 c} \operatorname{Re}(\alpha) I \quad (2.16)$$

The angle brackets explicitly denote a time average because the driving frequency, ω , is too rapid to account for an appreciable effect. The electric field's intensity has also been substituted as $I = 2\epsilon_0 c |\tilde{E}|^2$. Because of its conservative nature, the dipole force is then,

$$\mathbf{F}_{dip}(\mathbf{r}) = -\nabla U_{dip}(\mathbf{r}) = \frac{1}{2\epsilon_0 c} \operatorname{Re}(\alpha) \nabla I \quad (2.17)$$

Eq. 2.17 demonstrates that the dipole force is proportional to the gradient of the incident field's intensity. For a Gaussian beam, this force is strongest at the center and felt in a three-dimensional manner.

The expression for the dipole potential, Eq. 2.16, will be more useful if the atomic polarizability is explicitly defined. This is the point of the main classical consideration: take the electron, with mass m_e and elementary charge e , to be elastically bound to the atom with an oscillation frequency, ω_0 , equal to that of the optical transition frequency. The motion of this electron is damped due to the power radiated by an accelerated charge, $P = \frac{2}{3} \frac{e^2}{c^3} |\dot{\mathbf{v}}|^2$, known as Larmor's formula [33]. Then, using the standard equation of motion for a damped, driven oscillator, $\ddot{x} + \Gamma \dot{x} + \omega_0^2 x = \frac{-eE(t)}{m_e}$ with Γ denoting the radiative damping rate, an expression for the complex polarizability is available [17],

$$\alpha = \frac{e^2}{m_e} \frac{1}{\omega_0^2 - \omega^2 - i\omega\Gamma} \quad (2.18)$$

Now, Eq. 2.18 takes its place in Eq. 2.16 along with the assumptions made that saturation effects are negligible because of large detuning from resonance, $|\Delta| >> \Gamma$ and $\Delta \ll \omega_0$ where $\Delta \equiv \omega - \omega_0$, to obtain the desired equation for the dipole potential,

$$U_{dip}(\mathbf{r}) = \frac{3\pi c^2}{2\omega_0^3} \frac{\Gamma}{\Delta} I(\mathbf{r}) \quad (2.19)$$

An important conclusion to draw here is that the dipole potential is negative, as thus can act as a trapping potential, if the detuning of the laser, Δ is negative (red-detuned).

2.4.2 Multi-Level Atoms

The previous two-level classical derivation is actually a reasonably accurate approximation of the dipole potential in a FORT, but it does not include the additional effects seen in an interaction with multi-level atoms. Principally, the energy levels of the ground and excited states in the multi-level atom are shifted due to the intense far-off resonance light field. These energy shifts are small in reality when compared to the spacing of free-space atomic energy levels. Therefore, the effect of the light field on the atomic levels is treated as a second order perturbation of the electric field.

From the quantum mechanical viewpoint, an atom interacting with a electric field is described by a perturbation Hamiltonian of the form, $H' = \mu \cdot E$, where the electric dipole operator is defined, $\mu = -er$ and r is the relative electron position vector. The second order energy correction is, in general, given by [22],

$$E_i^{(2)} = \sum_{j \neq i} \frac{|\langle i^{(0)} | H' | j^{(0)} \rangle|^2}{(E_i^{(0)} - E_j^{(0)})} \quad (2.20)$$

where the superscripts indicate the perturbation order and $|i^{(0)}\rangle$ the unperturbed atomic states. For the unperturbed energies in the denominator of the sum in Eq. 2.20, the *dressed state* picture is used considering the atom and field photons together [34]. Following this view, the ground state atom has no internal energy, but the field has energy $n\hbar\omega$ depending on the number of photons present, n . When the atom absorbs one of these photons, it gains internal energy $\hbar\omega_0$, and the field loses a photon so it has energy, $(n - 1)\hbar\omega$. The denominator becomes,

$$\begin{aligned} E_i^{(0)} - E_j^{(0)} &= (n\hbar\omega) - [\hbar\omega_0 + (n - 1)\hbar\omega] \\ &= \hbar(\omega - \omega_0) = \hbar\Delta_{ij} \end{aligned} \quad (2.21)$$

Then for a two level atom with ground state labeled $|g\rangle$ and excited state labeled $|e\rangle$, the energy correction simplifies to,

$$E^{(2)} = \Delta E = \pm \frac{|\langle e | \mu | g \rangle|^2}{\Delta} |E|^2 = \pm \frac{3\pi c^2}{2\omega_0^3} \frac{\Gamma}{\Delta} I \quad (2.22)$$

where $\Gamma = \frac{\omega_0^3}{3\pi\epsilon_0 hc^3} |\langle e | \mu | g \rangle|^2$, and the $+$ denotes the excited state energy addition whereas the $-$ denotes the ground state energy subtraction. Note that this energy

shift (known as the *AC Stark shift*) that falls out of perturbation theory for the two-level atom is the same as previously derived, Eq. 2.19, but in the opposite direction for the excited state. The shifted energy levels are depicted in Fig. 2.4 for a general two-level atom.

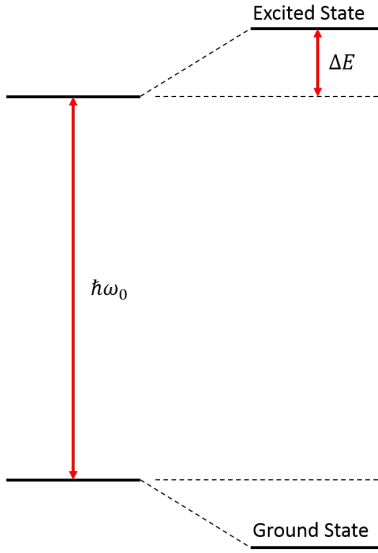


Figure 2.4: Far-off resonant light causes the energy levels of a two-level atom to be shifted by an amount, ΔE .

In a multi-level atom including the fine and hyperfine sublevel manifolds, the nondegenerate perturbation correction from Eq. 2.20 still holds if there are no couplings between degenerate sublevels [22]. This holds true if the polarizations of incident beams are assumed to pure, which in most experimental cases is close to reality. The goal is then to calculate light shifts (from the AC Stark shift) for each sublevel. Dipole matrix elements, $\mu_{ij} = \langle e_i | \hat{\mu} | g_i \rangle$, list out the coupling strength between particular states of the atom and the incident light field. These can be rewritten using the Wigner-Eckart Theorem [35] as a product of a Clebsch-Gordan coefficient, $\langle F, m_F | F', 1, m'_F, q \rangle$ and the reduced matrix element, $\langle F || \hat{\mu} || F' \rangle$ [23] where $|F, m_F\rangle$ specifies a hyperfine state, and $q = 0, \pm 1$ determines the polarization of the light (0 for linear, ± 1 for σ_{\pm}). Following [23], the reduced dipole matrix elements can be reduced further,

$$\langle F || \hat{\mu} || F' \rangle = \langle J || \hat{\mu} || J' \rangle (-1)^{F'+1+I} \sqrt{(2F'+1)(2J+1)} \left\{ \begin{matrix} J & J' & 1 \\ F & F' & I_N \end{matrix} \right\} \quad (2.23)$$

where I_N is the total nuclear angular momentum. The values of $\langle J || \hat{\mu} || J' \rangle$ may be

calculated from knowledge of the lifetime by [23],

$$\frac{1}{\tau_{JJ'}} = \frac{\omega_0^3}{3\pi\epsilon_0\hbar c^3} \frac{2J+1}{2J'+1} |\langle J||\hat{\mu}||J'\rangle|^2 \quad (2.24)$$

Now, a complete expression can be written for calculating any dipole matrix element,

$$\begin{aligned} \langle e_i | \hat{\mu} | g_i \rangle &= |\langle J || \hat{\mu} || J' \rangle| \\ &\times \left[\langle F, m_F | F', 1, m'_F, q \rangle (-1)^{F'+1+I} \sqrt{(2F'+1)(2J+1)} \begin{Bmatrix} J & J' & 1 \\ F & F' & I_N \end{Bmatrix} \right] \end{aligned} \quad (2.25)$$

The term in square brackets has been compiled in Ref. [23]. Now, it is straightforward to calculate the light shifts for any ^{85}Rb ground state, $|J, F, m_F\rangle$ to any excited state in hyperfine manifold, $|J', F', m'_F\rangle$ by using Eq. 2.20 and summing over all excited states, $|e_j\rangle$, in consideration. Knowing these light shifts is crucial to experiment. It allows for much needed accuracy when applying other laser beams to induce transitions of atoms while in the FORT. Thus, this type of calculation is used intensively throughout this work.

2.5 Single Atom Preparation through Light-Assisted Collisions

In the experimental process discussed in this thesis, once atoms are loaded into the FORT, the goal is to expel all but one with high repeatability so that experiments may be done on the single atom with reasonable efficiency. In a two-atom collision process, a situation in which only one is lost as a result would lead to such a deterministic single atom preparation. This can be realized by manipulating the atom-atom interaction such that one is transferred to an electronic excited as the collision occurs. This process is dubbed as a light-assisted collision and is employed throughout the following experiment. The following sections describe the semi-classical model behind this mechanism, which is represented schematically in Fig. 2.5

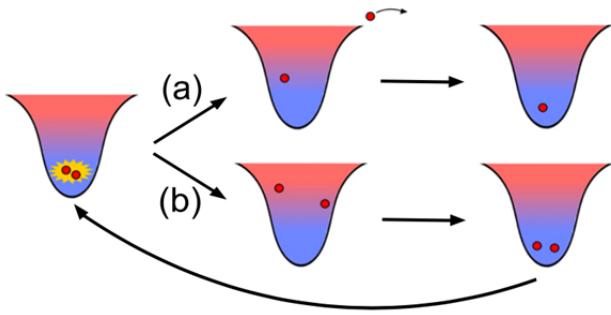


Figure 2.5: Light assisted collisions in a FORT may lead to (a), one atom expelled from the trap due to the energy gained in an inelastic collision or (b), both atoms retained in the trap after an elastic or minor inelastic collision. [36]

2.5.1 Long-Range Atomic Potentials

When examining atomic collisions in this manner, it is first important to set up a schematic picture of atoms interacting via potential functions as a function of internuclear separation, labeled R . In the ground state, the potential, $U_g(R)$, which is always attractive, can be expressed in a power series expansion of $\frac{1}{R}$ [37],

$$U_g(R) = -\frac{C_6}{R^6} - \frac{C_8}{R^8} - \dots \quad (2.26)$$

where C_6 is a coefficient from induced dipole-dipole interaction and C_8 from dipole-quadrupole interaction [37]. Clearly, at long range, when $R \rightarrow \infty$, $U_g(R)$ approaches $-\frac{C_6}{R^6}$. The two ground state atoms will be represented as $|S + S\rangle$ - see Fig. 2.6.

Analogously, the excited state atomic potentials are also shifted. When one atom of the colliding pair is excited, the potential will be represented as $|S + P\rangle$ (for alkali atoms) - see Fig. 2.6, and it can be expanded as a function of R [37],

$$U_e(R) = \hbar\omega_0 \pm \frac{C_3}{R^3} \pm \frac{C_5}{R^5} \pm \dots \quad (2.27)$$

where $\hbar\omega_0$ is the added energy of excitation, or the energy separation between ground and excited states. Here, the C_3 coefficient originates from resonant dipole interaction, and C_5 from resonant quadrupole interaction [37]. Because the asymptotic form of this potential is $\hbar\omega_0 \pm \frac{C_3}{R^3}$, and C_3 is from the resonant condition of the dipole interaction, the relative phase of each dipole dictates whether the potential is attractive or repulsive.

The two-atom quasimolecule will undergo a transition to some vibration-rotation level when exposed to a resonant optical field, frequency ω_L and the internuclear separation where this is most likely to occur is referred to as the Condon point, R_C [30]. It is the separation value where the laser frequency is resonant with the energy difference in the two-atom system. For a transition to the $|S + P\rangle$ state, this point is,

$$R_C = \left(\frac{C_3}{\hbar\Delta} \right)^{\frac{1}{3}} \quad (2.28)$$

where Δ is the difference in angular frequency of the optical field and the ground-excited energy difference, $\Delta = \omega_L - \omega_0$. Depending on the detuning, $\pm\Delta$, the transition of the quasimolecule will end in either the attractive (negative U_e), or repulsive (positive U_e) potential. Since blue-detuned light incurs a positive Δ term, it transfers the atoms to a repulsive potential, and vice versa for red-detuned light, as shown in Fig. 2.6.

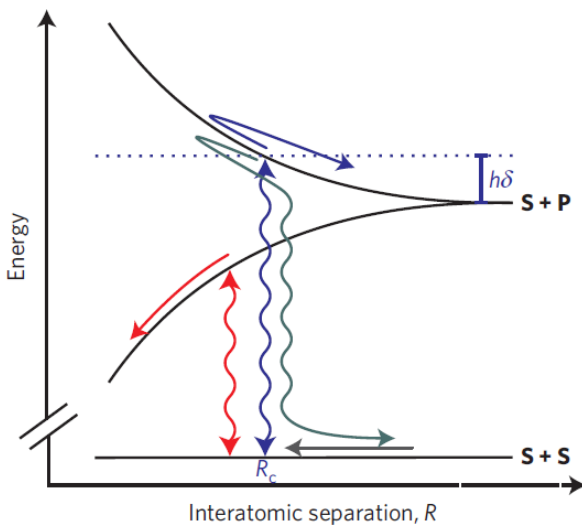


Figure 2.6: A potential curve model of one-dimensional light-assisted collisions: Two ground state atoms enter along the **gray** arrow. With incident blue-detuned light, the atoms transition along the **blue** arrow to an excited and repulsive potential, gaining maximum energy $\hbar\delta$. As the atomic separation nears R_C , elastic collisions lead to optical shielding of the energy transfer along the **green** arrow. With incident red-detuned light, the atoms transition along the **red** arrow to an attractive potential leading to pair loss from the trap. [38]

2.5.2 Landau-Zener Transition

The light-assisted collision process can be modeled using the Landau-Zener (LZ) avoided crossings picture, which details transition probabilities of dressed states [30, 39]. Now, the quasimolecular states will be labeled as dressed states, $|S + S, n\rangle$ and $|S + P, n - 1\rangle$, where n is the number of field photons. The term avoided crossing refers to the fact that the added energy of the coupling laser light introduces an interaction term in the Hamiltonian and separates the states at the Condon point. This is depicted schematically in Fig. 2.7 where the green dashed lines represent the states without added coupling light, and the blue curves show the dressed state energies.

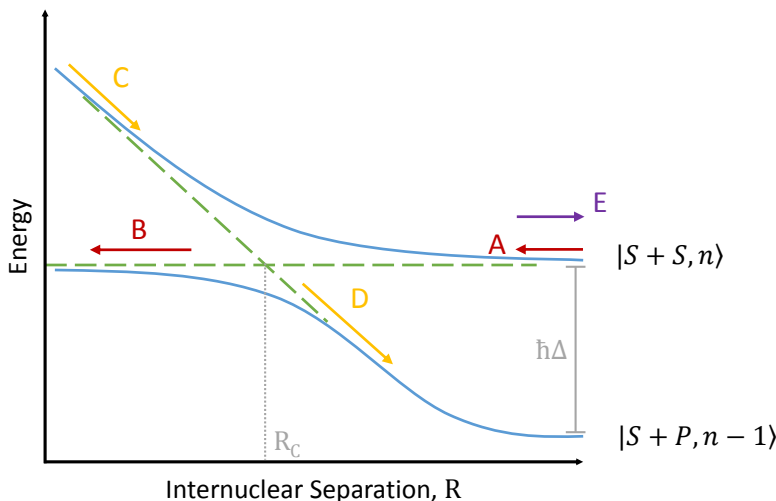


Figure 2.7: Schematic picture of the Landau-Zener avoided crossing description of light-assisted collisions. The **green** dashed lines and **blue** solid lines indicate the states' energies in the absence and presence of coupling respectively. The **red** arrows 'A' to 'B' symbolize a Landau-Zener transition from the ground to excited state, while the **yellow** arrows 'C' to 'D' represent the same transition after an adiabatic following along $|S + S, n\rangle$ through R_C . After entering along arrow 'A,' exiting on 'E' implies an elastic collision occurred, but exiting on 'D' implies an inelastic collision.

When atoms approach R_C on the $|S + S, n\rangle$ curve, there are two possible outcomes. They may move through the region relatively unaffected in an adiabatic following in which they stay on the same potential curve. They may also transition to the other dressed state potential with probability given by [30],

$$P_{LZ} = \exp\left(\frac{-2\pi\hbar\Omega^2}{v\alpha}\right) \quad (2.29)$$

where v is the relative radial atomic speed at R_C and Ω is the resonant Rabi frequency. Here, α is the potential slope difference at R_C . This needs to be rewritten in order for Eq. 2.29 to be pragmatic. Explicitly [40],

$$\alpha = \left| \frac{d[U_e(R) - U_g(R)]}{dR} \right|_{R_C} \approx -\frac{3C_3}{R_C^4} = \frac{3\Delta}{R_C} \quad (2.30)$$

Then the probability of a LZ transition occurring is,

$$P_{LZ} = \exp \left(\frac{-2\pi\Omega^2}{3v\alpha\Delta} \right) \left(\frac{C_3}{\hbar\Delta} \right)^{\frac{1}{3}} \quad (2.31)$$

The probability of adiabatic following occurring at the Condon point is then simply,

$$P_A = 1 - P_{LZ} \quad (2.32)$$

2.5.3 Repulsive Light-Assisted Collisions

With the models established, an analysis of what happens in the experimental situation is made clear in the case of repulsive (blue-detuned) light-assisted collisions in the FORT. Either an elastic or inelastic collision may take place depending on which potential curve the atoms exit the collision, i.e. move toward $R \rightarrow \infty$, after entering in the $|S + S, n\rangle$ state. Exiting on the same $|S + S, n\rangle$ potential curve implies that an elastic collision occurred because there was no net change in energy. This can happen if two successive LZ transitions occur - entering at arrow 'A', transitioning to arrow 'B,' changing directions and coming back out along arrow 'E' in Fig. 2.7 - with probability P_{LZ}^2 . Two successive adiabatic followings could also occur by entering along arrow 'A,' moving against arrow 'C,' changing directions and exiting along arrow 'E' in Fig. 2.7 with probability P_A^2 .

Exiting on the other channel, $|S + P, n - 1\rangle$, implies that an inelastic collision occurred because the atoms gain an energy $\hbar\Delta$. That is the energy difference between the asymptotic potential curves as shown in Fig. 2.7. This can happen when the atoms either undergo an adiabatic passage then LZ transition or the reverse. For example in Fig. 2.7, the atoms enter along arrow 'A,' make an LZ transition to arrow 'B,' and exit along arrow 'D' via adiabatic following. The probability of such a collision is $2P_A P_{LZ}$ picking up a factor of 2 because there are two possibilities. By tuning the laser frequency, or level of blue detuning, the energy gained by the atoms

in the inelastic collision is subsequently tuned. Then the depth of the FORT can be adjusted such that the energy gained by the pair will be enough for one atom to leave the trap but insufficient for both. This technique leads to near-deterministic preparation of atoms as seen in [38].

In the case of red-detuned light-assisted collisions, the amount of energy gained by the atoms cannot specifically be tuned in the same way. Instead, as seen in Fig. 2.6, the atoms are transferred to an attractive potential curve. Here, they may gain more kinetic energy than could be contained by the trapping potential. This mechanism often leads to pair loss. Consequently, the probability of a single atom being loaded into the FORT is $\sim 50\%$ depending on if the original number of atoms is even or odd [18].

3 | Ultracold Few-Body Systems

This chapter describes main theoretical background of this thesis, ultracold three-body interactions. Low energy scattering of two particles is first introduced followed by an explanation of inelastic three-body collisions. The discussion of basic two-body scattering aims to introduce concepts and terminology that are requisite to understanding the three-body system, namely the *s*-wave scattering length, a . A general discussion of wave scattering in the asymptotic form is presented followed by consequences arising from more realistic scattering situations.

Three-body recombination is a fundamental process which manifests itself throughout physics in ultracold plasmas [41], atmospheric chemistry [42], and even astrophysics [43]. Briefly, three bodies collide forming reaction products of a diatomic molecule (dimer) and free atom. Both the molecule and free atom gain the introduced binding energy causing all bodies to be lost from the trapping potential from the additional kinetic energy. In atomic species with a negative scattering length, such as ^{85}Rb , only tightly bound molecular states are possible, which is different from the potentially weakly bound states resulting from atoms with a positive scattering length.

The experimental setting of isolated ultracold atoms in a controllable state allows for the study of the recombination mechanism in an unprecedented fashion. Typically, this process is observed in an atomic ensemble through population measurements in a Bose-Einstein condensate. However, the experiment described in this thesis uniquely observes three-body recombination in a direct fashion. The population dynamics are discerned by preparing three separated single spin-polarized atoms, combining them into one potential well, allowing a set interaction time, then analyzing trap loss through a fluorescence signal. The system of equations that models this multi-decay process is also presented in this chapter.

3.1 Atomic Collisions

Given two distinguishable particles A and B with some interaction potential, initial state, energy, and momentum, (the initial wavefunction), the general goal is to predict the the energetic properties of the scattered wavefunction based on the scattering potential. The first step is to define their spatial coordinates, \mathbf{r}_A and \mathbf{r}_B , with masses M_A and M_B . Therefore, the relevant Schrödinger equation is,

$$\left[\frac{-\hbar^2}{2M_A} \nabla_A^2 + \frac{-\hbar^2}{2M_B} \nabla_B^2 + V(\mathbf{r}_A, \mathbf{r}_B) \right] \Psi(\mathbf{r}_A, \mathbf{r}_B) = E\Psi(\mathbf{r}_A, \mathbf{r}_B) \quad (3.1)$$

where $V(\mathbf{r}_A, \mathbf{r}_B)$ is the interaction potential. As a standard method, the relative and center-of-mass motions can be uncoupled with a reduction to an effective one-body problem where the distance between particles is $\mathbf{r} = \mathbf{r}_A - \mathbf{r}_B$, the center-of-mass position vector, $\mathbf{R} = \frac{M_A \mathbf{r}_A + M_B \mathbf{r}_B}{M_A + M_B}$, the reduced mass, $\mu = \frac{M_A M_B}{M_A + M_B}$, and the relative momentum, \mathbf{k} . (Note that in the case of this experiment, the ^{85}Rb atoms are indistinguishable bosons so $M_A = M_B$. The further consequences of indistinguishability will be discussed later in Sec. 5.4). The above form of the Schrödinger equation can then be split into angular and radial components. The radial equation is given as [22],

$$\left[\frac{-\hbar^2}{2\mu r^2} \frac{d}{dr} \left(r^2 \frac{d}{dr} \right) + \left(V(r) + \frac{\hbar^2 l(l+1)}{2\mu r^2} \right) \right] \psi(k, r) = E\psi(k, r) \quad (3.2)$$

where l is the angular momentum quantum number. The collision energy is given by,

$$E = \frac{\hbar^2 k^2}{2\mu} \quad (3.3)$$

3.1.1 Asymptotic Analysis

A general collision can be separated into three regions: input asymptote, interaction region, and output asymptote. The paths of the particles coming into and exiting the collision are approximately straight because of the relatively large separation distance between them. However, in the relatively short range separation region, the interaction between the particles becomes non-negligible and requires analysis of the possibly complicated dynamics. Then in practice, when seeking a mathematical

description of the entire process, it is easiest to simply deal with the asymptotic paths first and then consider the effects of the added interaction potential.

Without considering an interaction potential at first, i.e. $V = 0$, the plane wave form wavefunction for some internal state of the atoms, labeled $|0_A\rangle$ and $|0_B\rangle$, is,

$$\Psi(\mathbf{r}) = e^{i\mathbf{k}\cdot\mathbf{r}} |0_A 0_B\rangle \quad (3.4)$$

If the particles have no interaction, then their collision should result in some scattered wave with complex amplitude different than that of the incident. Evaluating this wavefunction at large r gives just that, a plane wave plus a scattered wave,

$$\Psi(\mathbf{r}) \sim \left[e^{i\mathbf{k}\cdot\mathbf{r}} + \frac{e^{ikr}}{r} f(E, \hat{\mathbf{k}}, \hat{\mathbf{k}}_s) \right] |0_A 0_B\rangle \quad (3.5)$$

where $\hat{\mathbf{k}}$ is the corresponding unit vector of \mathbf{k} , $\hat{\mathbf{k}}_s$ is the unit vector representing the scattered wave, and $f(E, \hat{\mathbf{k}}, \hat{\mathbf{k}}_s)$ is the scattered wave amplitude.

To make the analysis of the scattered wave more practical, it can be broken down into components of its angular momentum, or *partial waves*. The partial wave expansion of a plane wave is written as [30],

$$e^{i\mathbf{k}\cdot\mathbf{r}} = 4\pi \sum_{l=0}^{\infty} \sum_{m=-l}^l i^l Y_{lm}^*(\hat{\mathbf{k}}) Y_{lm}(\hat{\mathbf{k}}_s) j_l(kr) \quad (3.6)$$

where Y_{lm} is the spherical harmonic and the substituted j_l function has the asymptotic form,

$$j_l \sim \frac{\sin(kr - \frac{\pi}{2}l)}{kr} \quad (3.7)$$

Now, the wavefunction in Eq. 3.4 is rewritten with the expansion terms as,

$$\Psi(\mathbf{r}) = 4\pi \sum_{l=0}^{\infty} \sum_{m=-l}^l i^l Y_{lm}^*(\hat{\mathbf{k}}) Y_{lm}(\hat{\mathbf{k}}_s) \frac{F_l(E, r)}{r} |0_A 0_B\rangle \quad (3.8)$$

where $F_l(E, r)$ is the solution to the radial part of the Schrödinger equation, Eq. 3.2. Just looking at asymptotic solution, i.e. when $R \rightarrow \infty$, gives,

$$\frac{F_l(E, R)}{r} \sim \sin\left(kr - \frac{\pi}{2}l + \eta_l\right) \frac{e^{i\eta_l}}{kr} \quad (3.9)$$

where η_l is the phase shift induced by some interaction potential that may be present. The phase shift originates from the fact that the wavefunction is 'reflected' off a scattering potential surface.

There is an alternate method of connecting initial states to final scattered states via terms in a transfer matrix referred to as the scattering matrix method [44]. Its only relevance in this discussion is to readily write out the scattering amplitude from Eq. 3.5 also in terms of the partial wave expansion terms from above as [30],

$$f(E, \hat{\mathbf{k}}, \hat{\mathbf{k}}_s) = \frac{2\pi i}{k} \sum_{l=0}^{\infty} \sum_{m=-l}^l i^l Y_{lm}^*(\hat{\mathbf{k}}) Y_{lm}(\hat{\mathbf{k}}_s) T_l(E) \quad (3.10)$$

where $T_l(E)$ is a scattering matrix element equal to $1 - e^{2i\eta_l}$ [30]. Eq. 3.10 gives the energy (amplitude) of the outgoing wave from the interaction region, which was part of the goal of describing the asymptotic scattering process from the beginning. Now, the interaction region comes into the picture.

The interaction region can be outlined with the scattering cross section, $\sigma(E)$. Generally, it is the area in which the particles must meet in order to be scattered. Its determination comes from integrating the scattering probability amplitude over all possible scattering directions and initial values of momentum,

$$\sigma(E) = \int_{4\pi} \frac{d\hat{\mathbf{k}}}{4\pi} \int_{4\pi} d\hat{\mathbf{k}}_s |f(E, \hat{\mathbf{k}}, \hat{\mathbf{k}}_s)|^2 \quad (3.11)$$

With the scattering amplitude defined, this can be written in a much simpler form,

$$\begin{aligned} \sigma(E) &= \frac{\pi}{k^2} \sum_{l=0}^{\infty} (2l+1) |T_l(E)|^2 \\ &= \frac{4\pi}{k^2} \sum_{l=0}^{\infty} (2l+1) \sin^2 \eta_l \end{aligned} \quad (3.12)$$

Clearly, the phase shift induced by the interaction potential is an important parameter in describing the collision process, as it appears in the representation of the scattering amplitude, Eq. 3.10, and the scattering cross section, Eq. 3.12. Along with the phase shift, a key piece of information is the general length scale in which the scattering process takes place, called the scattering length, a_l . This is found by

examining the phase shift in the limit where $k \rightarrow 0$ [35],

$$\lim_{k \rightarrow 0} k^{2l+1} \cot \eta_l = -\frac{1}{a_l} \quad (3.13)$$

3.1.2 Scattering Length and Phase Shift

The magnitude and sign of the scattering length are of fundamental importance to collisional properties of ultracold atoms. This is because of its relation to the scattered wave phase shift, η_l , and the nature of the interaction potential. To illustrate this, the radial part of the Schrödinger equation (Eq. 3.2) is brought back into play with some clarifying substitutions. Namely, $V(r)$ becomes an 'effective potential',

$$U(r) = \frac{2\mu}{\hbar^2} V(r) \quad (3.14)$$

and the wavefunction is scaled by r , such that $\rho_l(k, r) = r\psi(k, r)$. Now, the radial Schrödinger equation reduces to the simpler form [35],

$$\left[\frac{d^2}{dr^2} + k^2 - \frac{l(l+1)}{r^2} - U(r) \right] \rho_l(k, r) = 0 \quad (3.15)$$

where the relation from Eq. 3.3 is still true.

To model a more pertinent scattering situation, consider only *s*-waves ($l = 0$) in the low energy limit of $k \rightarrow 0$. This is effectively an assertion of ultracold atoms. When the atoms are far apart, $U(r)$ is surely negligible, leaving Eq. 3.15 as,

$$\frac{d^2 \rho_0(r)}{dr^2} \approx 0 \quad (3.16)$$

with a clear solution of,

$$\rho_0 \approx Br + C \quad (3.17)$$

for some constants B and C . These constants are determined by comparing this solution to the same one was shown earlier in Eq. 3.9,

$$\rho_l(k, r) \sim \mathcal{C}_l(k) \sin \left[kr - \frac{1}{2}l\pi + \eta_l(k) \right] \quad (3.18)$$

where \mathcal{C}_l is a normalization constant. In the low energy assumption ($l = 0$), this

becomes [30],

$$\rho_0(k, r) = \mathcal{C}_0 k \cos \eta_0 \left(r + \frac{1}{k} \tan \eta_0 \right) \quad (3.19)$$

Then, the constant terms are $B = \mathcal{C}_0 k \cos \eta_0$ and $C = \mathcal{C}_0 k \cos(\eta_0) \frac{1}{k} \tan \eta_0$. Recall that this is the asymptotic solution. In the interaction region, the wavefunction exhibits some rapid oscillations because of the introduced finite range interaction potential (e.g. a one-dimensional square well). The oscillating wavefunction must be joined continuously with the linear asymptotic wavefunction at the edge of the interaction potential in order to represent a physical situation. The scattering length is more technically defined to be the intercept of the line that joins the two wavefunctions. From Eq. 3.20, finding the intercept gives the condition, $r = -\tan(\eta_0)/k$, and again in the low energy limit the scattering length becomes [30],

$$a_{l=0} = a \equiv - \lim_{k \rightarrow 0} \frac{\tan \eta_0}{k} \quad (3.20)$$

It is evident from the definition in Eq. 3.20 that a_0 is undefined at $\eta_0 = \pm(n + \pi/2)$ for $n = 0, 1, 2, 3, \dots$, referred to as zero-energy resonances. For a potential well that is defined in a range (in one dimension) comparable to the scattering length (and 0 beyond that), these divergences in a exactly correspond to the appearance of possible bound states in the well [30]. When the well is too shallow to support any bound states, a is negative. As the well deepens enough to support one bound state, a diverges and reappears positive. It then passes smoothly through 0 to a negative value coming up to the point of two possible bound states, where it diverges again to reappear positive.

Furthermore, information about the sign of the scattering length, which is related to the scattered phase shift, alongside information about the interaction potential gives an explanation as to the stability of a BEC with such properties. Atomic species with a negative scattering length, a imply that the scattering phase shift η_0 forces the scattered wavefunction closer to the point of scattering (approximately the scattering length). This means that in a collection of identical atoms, i.e. in a BEC, two atoms have a higher probability of being found in the same location than in the positive a case, sparking ultimately destabilizing collisions [30]. The topic atom of this thesis, ^{85}Rb , has a negative scattering length, and thus in typical experimental conditions forms an unstable BEC [6].

3.2 Three-Body Interactions

Similar to the two-body scenario, the aim of analysis in a three-body interaction is to predict the outcome of a collision by analyzing a reduced wavefunction coming from the few-body Schrödinger equation in a landscape of potential energies. A major complication arises with the additional atom due to the existence of multiple possible outcomes, or fragmentation channels, in the collision. There are three possibilities in which the interaction could result in a dimer and a free atom, referred to as three-body recombination, owing to the three combinations of the atoms. One channel exists where the results are three free atoms. Most importantly from the following derivation comes the calculated rate of three-body recombination, labeled K_3 . This will be the theoretical basis for the rate at which three-body inelastic events occur in an experimental situation. There are multiple techniques to analyze a three-body system, including the Fadeev equations [45] and the Alt-Grassberger-Sandhas equations [46], but the method presented here appears to be the most common and compact - the adiabatic hyperspherical representation.

3.2.1 Hyperspherical Coordinates

Following the previous section, the coordinates of the three atoms in question can be defined by separating the center-of-mass and relative motions. The most pragmatic and popular coordinate system used to do this is referred to as hyperspherical coordinates and was first developed by Delves in the context of nuclear physics [47, 48]. Jacobi coordinates are defined as relative position vectors between the three atoms where a vector, ρ_{ij} connects two, and another vector, ρ_{ijk} points from the center of mass of atoms i and j to the remaining atom, k . The possible values of

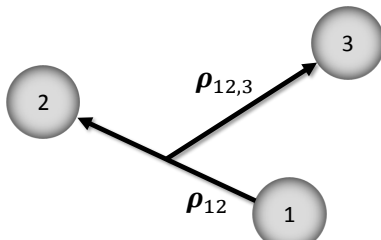


Figure 3.1: Diagram of Jacobi coordinates in a three-body system.

i, j, k are 1, 2, 3, of which permutations must be kept in mind when ultimately dealing with identical atoms. Then, reduced masses can be written [47, 48],

$$\mu_{ij} = \frac{m_i m_j}{m_i + m_j}, \quad \mu_{ij,k} = \frac{m_k(m_i + m_j)}{m_i + m_j + m_k} \quad (3.21)$$

and,

$$\mu_3 = (\mu_{ij}\mu_{ij,k})^{\frac{1}{2}} = \left(\frac{m_1 m_2 m_3}{m_1 + m_2 + m_3} \right)^{\frac{1}{2}} \quad (3.22)$$

It will be convenient later when expressing kinetic energy terms if the position vectors are scaled by these reduced masses,

$$\begin{aligned} \boldsymbol{\rho}_{ij} &= \sqrt{\frac{\mu_{ij}}{\mu_3}} (\mathbf{r}_i - \mathbf{r}_j) \\ \boldsymbol{\rho}_{ij,k} &= \sqrt{\frac{\mu_{ij,k}}{\mu_3}} \left(\mathbf{r}_k - \frac{m_i \mathbf{r}_i + m_j \mathbf{r}_j}{m_i + m_j} \right) \end{aligned} \quad (3.23)$$

Analogously to spherical coordinates, the overall size of the three-body system is described by one variable, the hyperradius R ,

$$R = \sqrt{\rho_{ij}^2 + \rho_{ij,k}^2} \quad (3.24)$$

The other five necessary coordinates are 'hyperangles' with no unique definition and collectively labeled Ω . It turns out that for any specific choice of hyperangle definition, the few-body Schrödinger equation can be established [49],

$$\left(-\frac{1}{2\mu_3} \frac{\partial^2}{\partial R^2} + \frac{\Lambda^2 + \frac{15}{4}}{2\mu_3 R^2} + V \right) \psi(R, \Omega) = E \psi(R, \Omega) \quad (3.25)$$

where the wavefunction is scaled by $R^{5/2}$, V is the total potential from interatomic interaction and Λ^2 is the hyperangular kinetic energy, which does depend on the specific choice of hyperangle. Delves originally defined the hyperangles in a simple way, as two sets of spherical angles and the angle between position vectors [47], but imposing permutation symmetry is ultimately challenging using these. The wiser choice for three identical atoms are the democratic hyperangles [50], which are built from the principal moments of inertia in the system. This set of angles includes the Euler angles from classical mechanics - yaw, pitch, and roll - and two other hyperangles, θ and φ , one of which is permutation invariant [51]. θ and φ are defined

using the interatomic spacing, r_{ij} , as [49],

$$r_{ij} = \frac{d_{ij}R}{\sqrt{2}}[1 + \sin \theta \cos(\varphi + \varphi_{ij})]^{\frac{1}{2}} \quad (3.26)$$

where,

$$d_{ij}^2 = \frac{m_k(m_i + m_j)}{\mu_3(m_i + m_j + m_k)} \quad (3.27)$$

and,

$$\tan\left(\frac{\varphi_{12}}{2}\right) = \frac{m_3}{\mu_3}, \quad \varphi_{23} = 0, \quad \tan\left(\frac{\varphi_{31}}{2}\right) = -\frac{m_2}{\mu_3} \quad (3.28)$$

for the angular ranges, $0 < \varphi_{12} < \pi$ and $\pi < \varphi_{31} < 2\pi$. A mapping of these bounded hyperangles is seen in Fig. 3.2

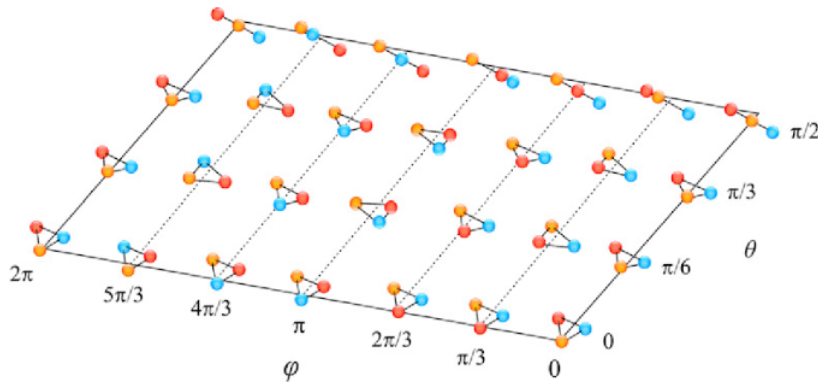


Figure 3.2: Atomic layout of the ranges of hyperangles θ and ϕ in the democratic coordinate system. Colors represent atom index and are arbitrary. [49]

3.2.2 Adiabatic Representation

With the coordinates defined, the Schrödinger equation, Eq. 3.25, can be solved for a specified interatomic potential. This is a challenging computation because of its six-dimensional order. Reducing this problem down to coupled one dimensional equations is thus a useful idea. In a similar manner to the Born-Oppenheimer separation for diatomic molecules [35], this simplification is done by holding R fixed, or treating it as an adiabatic variable, and solving the 'adiabatic equation' for all R . That is given as [49],

$$H_{ad}\Phi_\nu(R, \Omega) = U_\nu(R)\Phi(R, \Omega) \quad (3.29)$$

where the eigenstates $\Phi(R, \Omega)$ are the possible fragmentation channel functions of the collision, and the eigenvalues U_ν are the three-atom adiabatic potentials. The U_ν curves determine the hyperradial motion of the atoms by setting the energy landscape within which they move. Any necessarily labeled quantum numbers and channels are packaged into the subscript ν . The adiabatic Hamiltonian, H_{ad} , is written as,

$$H_{ad} = \frac{\Lambda^2}{2\mu_3 R^2} + V(R, \Omega) \quad (3.30)$$

similar to its previous definition in Eq. 3.25. V here is assumed to be a pairwise sum of the possible atomic interactions, $V(R, \Omega) = v(r_{12}) + v(r_{23}) + v(r_{31})$. Note that the hyperangles, Ω , are bounded such that the eigenvalues (adiabatic potentials) are discrete. Then at each R , the channel functions form a complete set, which means the total wavefunction can be expanded over the basis of eigenfunctions [49],

$$\psi(R, \Omega) = \sum_\nu F_\nu(R) \Phi_\nu(R, \Omega) \quad (3.31)$$

The expansion coefficients, $F_\nu(R)$, introduced here are the atomic hyperradial wavefunctions in some state, ν , which are analogous to the radial wavefunction, $\rho_l(k, r)$ from the two-atom scenario. In fact, once the channel functions, $\Phi(R, \Omega)$, and potentials, U_ν are known, then the three-atom problem is very similar to the two-atom case with the radial Eq. 3.15. Instead, one needs to solve the *hyperradial* Schrödinger equation [52],

$$\left[-\frac{1}{2\mu_3} \frac{d^2}{dR^2} + W_\nu(R) \right] F_\nu(R) - \frac{1}{2\mu_3} \sum_{\nu'} W_{\nu\nu'} F_{\nu'}(R) = E F_\nu(R) \quad (3.32)$$

The hyperradial wavefunctions, $F_\nu(R)$ resulting from this equation will describe the hyperradial motion of the atoms when in interacting within effective potentials, $W_\nu(R)$ (as in the two-body case). The difference from the two-atom radial equation is the introduction of non-adiabatic coupling terms, $W_{\nu\nu'}$ [53, 54].

3.2.3 Three-Body Recombination

Knowledge of the effective potentials, W_ν , gives the possible behavior of the colliding atoms when they have approached within a significant separation, R . There are three regions to consider in the potential landscape, as first described by Efimov

[55]. As shown in Fig. 3.3, these regions are the asymptotic long-range, $R \rightarrow \infty$, the scale-invariant, or ‘Efimov region,’ $R \sim |a|$, and the short range regime, $R \lesssim r_0$. This discussion is only concerned with low-energy atoms satisfying the condition of $|a| \gg r_0$ where r_0 is the range of atomic interaction. The red arrow in Fig. 3.3

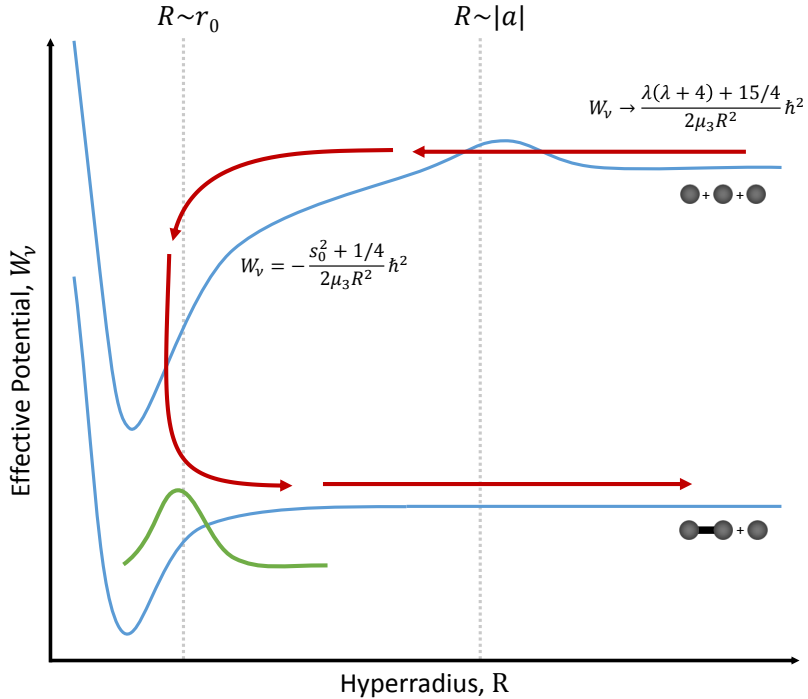


Figure 3.3: Diagram of hyperspherical effective potential curves. The **red** line traces the path of three-body recombination demonstrating the hyperradial wave motion along the **blue** effective potential curves. The **green** curve represents the repulsive barrier in the short-range regime seen in the convergence of W_ν . Adapted from [49]

depicts a general process of recombination. Sufficiently cold atoms incident from $R \rightarrow \infty$ first need to tunnel through a repulsive potential barrier to reach the range of $R \sim |a|$. Here, depending on the amplitude of the wavefunction, the atom may ‘roll down’ the potential well into the short-range region, $R \lesssim r_0$. In this regime, there is a probability of coupling into the deeply bound molecule and free atom state via a non-adiabatic driving transition. That is the outcome of interest, as it signifies three-body recombination has occurred. By understanding the hyperradial equations of motion and the probability of coupling into the recombination channel, the rate constant of three-body recombination, K_3 , can be determined.

Asymptotic Behavior

Outside of the initial potential barrier in Fig. 3.3, in the long-range region where $R \rightarrow \infty$, the solutions to the Schrödinger equation are just those of the free atoms with Hamiltonian,

$$H_{ad} = \frac{\Lambda^2}{2\mu_3 R^2} \quad (3.33)$$

As discussed extensively by Avery [56], the channels asymptotically go to hyperspherical harmonics, and the potentials in this region have the following asymptotic behavior,

$$W_\nu(R) \rightarrow \frac{\lambda(\lambda+4) + \frac{15}{4}}{2\mu_3 R^2} \hbar^2 \quad \text{for } \lambda = 0, 1, 2, 3, \dots \quad (3.34)$$

At ultracold temperatures, Esry et. al. showed that only the lowest continuum function, $\lambda = 0$, need be included in the analysis, as it governs the energy dependence of the recombination rate near zero energy [57]. In other words, only the lowest energy term in the free-particle wavefunction contributes to the recombination process. The hyperradial solutions in the long-range asymptote, i.e. the free-atom solutions, are Bessel functions [49]

$$F_\nu(R) \approx F_0(R) = R^{\frac{1}{2}} [AJ_{\lambda+2}(kR) + BN_{\lambda+2}(kR)] \quad (3.35)$$

where $k = \sqrt{2\mu_3 E}$, and A and B are constants pertaining to some set of specifically imposed boundary conditions.

Intermediate and Short-Range Behavior

The hyperradial wave that has tunneled into the intermediate region, where $R \sim |a|$ in Fig. 3.3, and traverses into the short range region, $R \lesssim r_0$, has a finite probability of exiting the process as a deeply bound diatom and a free atom (the lower effective potential curve in Fig. 3.3). Exiting the collision process on that curve implies that three-body recombination occurred.

There exist many other deeply bound two-body states into which two of the atoms could potentially couple, but actually the effects from all of them on three-body observable variables can be packaged into one 'inelasticity parameter,' η_* [58]. Furthermore, only the lowest effective potential curve need be considered in the collision process, as represented in Fig. 3.3. This is due to the fact that all three atoms must approach each other within the range of atomic interaction, a distance of

r_0 or smaller. Clearly this is true for the two atoms which form the dimer, but also for the third free atom. The only way that it could deliver enough momentum transfer to the molecule to conserve the momentum of the system overall is if it enters a region of r_0 or smaller. This means the hyperradius, R needs to shrink to order r_0 or below, which is only possible in the lowest order effective potential [58].

The form of the lowest effective potential in the scale-invariant region, $R \sim |a|$, and into the region of interaction, $R \sim r_0$ is a remarkably simple $1/R^2$ dependence [59],

$$W_\nu(R) = -\frac{s_0^2 + \frac{1}{4}}{2\mu_3 R^2} \hbar^2 \quad (3.36)$$

where $s_0 = 1.00624$ is a universal constant first derived by Efimov [60]. The value for s_0 arises from the Efimov effect. It is the fact that a system of three bosons has an infinite series of weakly bound states in the region where the scattering length, a , of two of the atoms approaches ∞ . The three-body bound states have a geometrical series of binding energies, $E_N \sim \exp(-2\pi N/s_0)$ for $N = 0, 1, 2, \dots$. Wang et. al. showed that this lowest effective potential, Eq. 3.36, is ultimately a convergence of all effective potentials at small R when additional deeply bound molecular states are included in the analysis. Moreover, the converging potentials display a universal repulsive barrier, as shown by the green curve in Fig. 3.3, near the range of the van der Waals interaction [59]. That prevents most extremely short-range interactions, $R \ll r_0$ in ultracold molecules that would be interaction-specific from occurring. The repulsive barrier is a surprising effect and a necessary inclusion to the effective potential picture in the short-range region. It in effect serves as a source for the studies of universality in interacting three-body systems [58, 59].

Recombination Rate

The properties of the effective hyperspherical potentials, as described above in each region of Fig. 3.3, dictate the nature of the three atoms during a collision when R is changing. In order to show this behavior in an experimental situation, there needs to be an observable variable from the collision. Here, that is the three-body recombination rate constant, K_3 . This rate can be defined basically as the relative amount of scattered flux out of the short-range region on the lowest effective potential curve. Though a more rigorous definition and derivation from Braaten et. al. shows that the rate constant is a sum of scattering matrix terms coming from a modified version of Efimov's radial law [58].

Efimov's namesake radial law came from the strategy of analytically solving the hyperradial equation, Eq. 3.32, in the scale-invariant, or intermediate, region and connecting the boundary conditions that all hyperradial waves entering the short range region are completely reflected back out to the long range region [55]. This assumption does not include the existence of coupling into the deeply bound molecular states, which allows for three-body recombination in atoms with $a < 0$. In reality, the probability of the incident hyperradial wave being reflected from the short-range region back to the long-range region is less than 1 and is equal to $e^{-4\eta_*}$ [58].

As a simplified description, K_3 arises from the contributions of the scattering matrix terms which connect incoming low-energy free atomic states to outgoing atom-dimer high-energy states in the asymptotic exiting regime [58]. This is essentially the scattering states which follow the red arrow in Fig. 3.3. The inelasticity parameter, η_* , that controls the probability of reflection from the short-range to the long range is very important to this calculation from qualitative reasoning alone. For atoms with negative scattering lengths, K_3 is given as [58],

$$K_3 = \frac{4590 \sinh(2\eta_*)}{\sin^2[s_0 \ln(a/a_-)] + \sinh^2 \eta_*} \frac{\hbar a^4}{m} \quad (3.37)$$

where a_- indicates the position of an Efimov resonance in terms of scattering length. Such a resonance occurs when an Efimov state becomes degenerate in the collision energy threshold [55], and enhanced three-body recombination is seen at these points [58, 61, 62]. Eq. 3.37 gives the three-body event rate constant for noncondensed atoms.

3.2.4 Theoretical Prediction of Three-Body Recombination Rate

Obtaining Eq. 3.37 was the goal of the Sec. 3.2 because it provides a theoretical calculation of the three-body recombination rate, K_3 , that is measured experimentally in this thesis. A theoretically calculated value for K_3 , denoted K_3^{th} , using the parameters of this experimental setting thus serves as a point of comparison for the later discussed experimental result, labeled K_3^{exp} .

The two-body scattering length, a , has been a prominent variable in this discussion of scattering theory thus far, as its tuning can lead to resonant phenomena in a two-or three-body system. Experimentally, it is then very useful to know this variable

precisely and have control over it. By operating in a magnetic regime that includes a Feshbach resonance, the scattering length can be tuned using a simple dependence on the magnetic field, B [63],

$$a(B) = a_{bg} \left(1 - \frac{\Delta}{B - B_{peak}} \right) \quad (3.38)$$

A Feshbach resonance refers to the resonant coupling that can occur between two colliding atoms and a molecular bound state of an interatomic potential. Here, B_{peak} represents the peak position of the Feshbach resonance, identified by a diverging scattering length ($a \rightarrow +\infty$), Δ denotes the width of that resonance, i.e. $\Delta = B_{a=0} - B_{peak}$ where $B_{a=0}$ is the necessary field for a to cross 0, and a_{bg} is the background scattering length. The term background specifies that a_{bg} is associated with the molecular potential curve at large internuclear distances, which is also referred to as the entrance channel in the terminology of Feshbach resonances. For ^{85}Rb atoms in the $|F, m_f\rangle = |2, -2\rangle$ state, Claussen et. al. measured $a_{bg} = -443(3)a_0$, $B_{peak} = 155.041(18)$ G, and $\Delta = 10.71(2)$ G [64]. With this information, a scattering length can be easily calculated for any applied magnetic field value, B using Eq. 3.41.

As described later in Sec. 5.4, there is a small magnetic bias field applied to the atoms of $B = 7.50 \pm 0.01$ G in this experiment. Using Eq. 3.38 alongside the results of Claussen et. al. [64], a scattering length for the ^{85}Rb atoms in this system is calculated as $a = -475a_0 \pm 3a_0$. Then, the relation in Eq. 3.37 for the three-body recombination constant, K_3 , for noncondensed atoms of negative scattering length is calculated using the parameters determined in [61] to be $K_3^{th} = (7.47 \pm 0.51) \times 10^{-25}$ cm⁶/sec. This value is set to be the theoretical basis for these experimental conditions. Note that the units of cm⁶/sec signify the radial scattered flux six-dimensional hyperspherical coordinate space.

3.3 Modeling Population Dynamics

The theoretical framework for K_3 described in this chapter is valuable because it expresses the three-body loss observable from base concepts of a few-body system. However, until the experiment in this thesis, three-body loss has not been observed directly on the few-atom scale but rather as population loss from a Bose-Einstein condensate (BEC). This experimental method is certainly useful. For example, with

this technique, inelastic collisions have been shown to be enhanced near Feshbach resonances, which ultimately destabilizes BECs with atoms of negative scattering length [7, 65]. Although, the approximate nature of the modeling used in the measurements of the inelastic loss processes in this context inherently blurs the underlying mechanisms. With a more direct and simple experiment of few-atom processes comes a more direct and ultimately more descriptive model. Both strategies of modeling are discussed in the following sections.

3.3.1 Model of Loss from BEC

In a BEC, the rate at which inelastic two- and three-body collisions cause population loss depends on the density profile of the atomic ensemble. This is typically modeled by a standard loss-rate equation that tracks the atom number, N , as a function of time [7],

$$\dot{N} = -K_2 \langle n \rangle N - K_3 \langle n^2 \rangle N - \frac{N}{\tau} \quad (3.39)$$

where $\langle n \rangle = \frac{1}{N} \int n^2(\mathbf{x}) d^3x$ and $\langle n^2 \rangle = \frac{1}{N} \int n^3(\mathbf{x}) d^3x$. The background loss rate, or one-body loss rate, is represented by τ . Note that this equation defines the rate constants as atom-loss rates. More commonly, rate constants are given as tracking events. In the case of K_3 as an event rate constant, a factor of three need be included to signify all three atoms being lost in an event, i.e. $\frac{dN}{dt} = -3K_3 \langle n^2 \rangle N$ [61].

Altin et. al. extend this model to dictate that the density is given by the modulus squared of the ground-state harmonic oscillator wave-function in the limit $a \rightarrow 0$. Then in the Thomas-Fermi limit, $N \frac{a}{a_{ho}} \gg 1$, the loss-rate equation evaluates to [66],

$$\dot{N} = -\frac{N}{\tau} - \gamma_2 K_2 N^{\frac{7}{5}} - \gamma_3 K_3 N^{\frac{9}{5}} \quad (3.40)$$

with,

$$\gamma_2 = \frac{15^{\frac{2}{5}}}{14\pi a^{\frac{3}{5}} a_{ho}^{\frac{12}{5}}} \quad \text{and} \quad \gamma_3 = \frac{5^{\frac{4}{5}}}{56\pi^2 3^{\frac{1}{5}} a^{\frac{6}{5}} a_{ho}^{\frac{24}{5}}} \quad (3.41)$$

where the subscript ho signifies harmonic oscillator. Each of the experiments that measure K_3 use a ^{85}Rb BEC [7, 66], and the only other documented measurement of K_3 for ^{85}Rb extracts the rate constant in the same manner but fits the measured K_3 vs. a using the theoretical model detailed above [61]. This loss rate model assumes

that the density profile of the BEC is fixed during the population decrease. That is not an accurate assumption, as the cloud certainly changes shape and density when atoms exit from it. To include a dynamic density profile in such a model may well be possible, but in any sense requires some assumption and creates a more challenging computation.

3.3.2 Direct Atom Triad Loss Model

The experiment described in this thesis is unique because it determines the three-body recombination rate coefficient on the basis of a pure few-body system. That means three-, two-, and one-atom loss events are directly observed from an initial population of three atoms confined in a trapping potential. This experimental scheme allows for a great simplification of the necessary modeling of three-body loss in an atomic system. Instead of using the possibly complicated tools needed to describe the dynamic density profile of a BEC, a system of linear population decay equations can fully describe the changing population of a few-body system:

$$\begin{aligned}\dot{N}_3(t) &= -\gamma_3 N_3 - \gamma_2(3N_3) - \gamma_1(3N_3) \\ \dot{N}_2(t) &= -\gamma_2 N_2 - \gamma_1(2N_2) + \gamma_1(3N_3) \\ \dot{N}_1(t) &= -\gamma_1 N_1 + \gamma_2(3N_3) + \gamma_1(2N_2) \\ \dot{N}_0(t) &= \gamma_3 N_3 + \gamma_2 N_2 + \gamma_1 N_1\end{aligned}\tag{3.42}$$

Here, N_i represents the population of i atoms observed in the FORT. γ_i denotes the loss rate for i -atom loss. As an example, the second equation in the set can be described in words as,

The change in two-atom population observation in the FORT as a function of time is dictated by (1) a negative contribution from a two-atom loss mechanism, (2) a negative contribution by two possibilities of a single-atom loss mechanism, and (3) a positive contribution from three possibilities of single atom loss events' effect on the three-atom population.

The solutions to this system of differential equations are simply sums of exponential terms,

$$N_3(t) = A \exp[-(\gamma_3 + 3\gamma_2 + 3\gamma_1)t] \quad (3.43a)$$

$$N_2(t) = \frac{-3A\gamma_1}{\gamma_3 + \gamma_2 + \gamma_1} \exp[-(\gamma_3 + 3\gamma_2 + 3\gamma_1)t] + B \exp[-(\gamma_2 + 2\gamma_1)t] \quad (3.43b)$$

$$N_1(t) = -\alpha \exp[-(\gamma_3 + 3\gamma_2 + 3\gamma_1)t] - \beta \exp[-(\gamma_2 + 2\gamma_1)t] + C \exp(-\gamma_1 t) \quad (3.43c)$$

$$\begin{aligned} N_0(t) = & \left[-\gamma_3 A + \left(\frac{3A\gamma_1\gamma_2}{\gamma_3 + 2\gamma_2 + \gamma_1} \right) + \gamma_1 \alpha \right] \left(\frac{1}{\gamma_3 + 3\gamma_2 + 3\gamma_1} \right) \exp[-(\gamma_3 + 3\gamma_2 + 3\gamma_1)t] \\ & + (-\gamma_2 B + \gamma_1 \beta) \left(\frac{1}{\gamma_2 + 2\gamma_1} \right) \exp[-(\gamma_2 + 2\gamma_1)t] - C \exp(-\gamma_1 t) + D \end{aligned} \quad (3.43d)$$

where,

$$\begin{aligned} \alpha &= \left(\frac{3A}{\gamma_3 + 3\gamma_2 + 2\gamma_1} \right) \left[\gamma_2 - \left(\frac{2\gamma_1^2}{\gamma_3 + 2\gamma_2 + \gamma_1} \right) \right] \\ \beta &= \left(\frac{2B\gamma_1}{\gamma_2 + \gamma_1} \right) \end{aligned} \quad (3.44)$$

and A , B , C , and D are constants of integration found from initial populations at $t = 0$. Appendix A gives the explicit derivation of these solutions.

With the ability to count the number of atoms, $N_i(t)$ in the FORT at varying times, t , the linear rate constants, γ_i , can be extracted from fitting experimental data to the above solution set. Then, relating K_3 to γ_3 (see Sec. 6.1.2) produces a more straightforward measurement method than from BEC population loss. The remainder of this thesis discusses the experiment used to measure K_3 in ^{85}Rb using this model.

4 | Experimental Apparatus

This chapter illustrates the structure of the experimental apparatus used to prepare the single ^{85}Rb single atoms discussed throughout this thesis. The systems described here were originally constructed by previous PhD students and postdoctoral fellows (see Sec 1.2) within this research group, but they require diligent maintenance and adaptation for consistent functionality. Since the isolation of single atoms is the backbone of the experiment presented beyond this chapter, it is important to describe the mechanics of the process.

First, the vacuum chamber, which serves as the site of all experiments, is detailed followed by a discussion of each laser system used. This includes the lasers and magnetic fields used to trap, cool, and image single atoms. The chapter concludes with an outline of the methods used to synchronize and control each stage of the experimental sequence.

4.1 Fundamental Setup

4.1.1 Vacuum System

In order to minimize unwanted interactions with the environment, experimental procedures involving atomic control must be performed inside an ultra-high vacuum system chamber. Its schematic is seen in Fig. 4.1. It is broken into two main sections: the reservoir chamber and the science chamber.

The duty assigned to the reservoir chamber is to supply the science chamber with ^{85}Rb atoms in gaseous form. Natural Rubidium occurs as a soft metal comprised of 72.2% ^{85}Rb and 27.8% ^{87}Rb [23], and a 1g sample of this is placed in the reservoir chamber. There are two valves separating the solid Rubidium and the differential tube leading directly into the science chamber (represented as the thin channel leading "To Reservoir Chamber" in Fig. 4.1). The first valve allows for the isolated heating

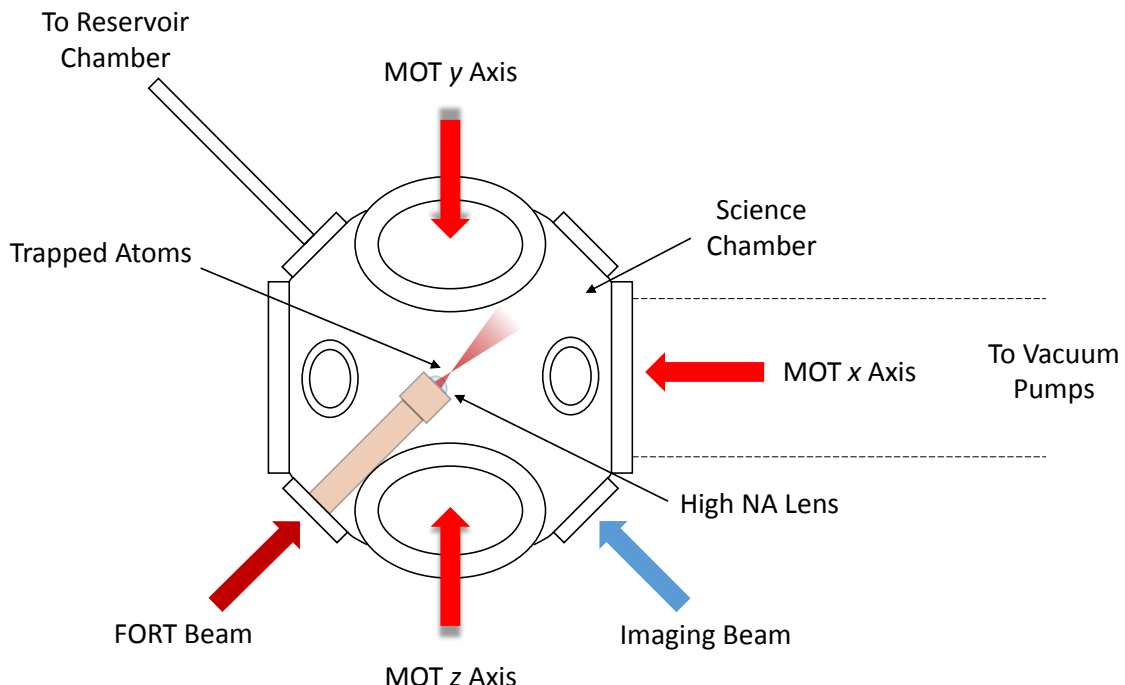


Figure 4.1: Side-view of the science chamber with MOT axes for reference.

and sublimation of the rubidium sample in its housing by a thermoelectric device. The space between the two valves allows for a turbo-molecular pump to be connected and create the initial vacuum pressure ($\sim 10^{-8}$ Torr) as well as an ion pump to further the vacuum. Once the vacuum is established and the second valve is opened, the free atoms move through the differential tube into the science chamber.

The science chamber is a spherical cube with 14 total view ports, 13 of which are anti-reflection coated so that laser beams may pass through unaffected. The remaining port serves as a mount for a custom brass claw lens holder. It holds a high numerical aperture (NA) lens - working distance = 2.9 mm - that focuses the incoming FORT beam to a necessarily small spot size. As labeled in Fig. 4.1 ("To Vacuum Pumps"), another arm is connected to the science chamber. This allows connections for another ion pump, a Titanium sublimation pump, and an ion gauge. The ion pump, along with the other one in the reservoir chamber, creates the initial 'high' vacuum, which is improved by about 4 orders of magnitude when the sublimation pump is fired. All pressure sensing is done by the ion gauge. In order to maintain a well functioning MOT system, it is crucial to have a reliably low vacuum pressure; in this experiment, the pressure stays near 4×10^{-11} Torr. This corresponds to trapped atom lifetime of approximately 60 seconds.

4.1.2 Magneto-Optical Trap

The larger 6 of the view ports also act as mounts for the magnetic quadrupole field-forming coils necessary for MOT operation. Running current as in an anti-Helmholtz configuration, these coils create a magnetic field gradient of $dB/dz = 7.7 \text{ Gcm}^{-1}$ in along the MOT z axis and 3.8 Gcm^{-1} on the other two axes. The orientation of the MOT axes relative to the geometry of the science chamber and FORT beam is shown in Fig. 4.1.

MOT Laser

The beams used for cooling in the MOT come from an external cavity diode laser source at 780nm. The principal frequency of the laser is precisely set using a saturated absorption locking scheme. This involves passing two overlapping beams, a saturating pump beam and an offsetting probe, through a Rubidium gas cell, detecting the signal, and feeding back a control voltage to prevent frequency drift from thermal expansion within the laser cavity. The term saturated absorption refers to the technique of resolving hyperfine spectral lines within the Doppler broadened absorption profile of a typical gas cell [67]. The locking point used here is the crossover peak between the $F = 3$ to $F' = 3$ and $F = 3$ to $F' = 4$ D2 hyperfine lines in ^{85}RB (see Fig. 4.2). This is due to the fact that it is clean signal to use in the locking scheme that is near the $F = 3$ to $F' = 4$ D2 transition, which is employed as the main cooling transition.

Acousto-Optical Modulator Control

The laser light of the MOT cooling beams is used in multiple stages of the experiment and thus requires efficient tuning of frequency and power to accommodate different experimental functions. Frequency and power shifts are fulfilled in this case by passing the light through an acousto-optical modulator (AOM) in a double-pass configuration. An AOM is a device consisting of a transparent crystal with an attached piezoelectric transducer. When the transducer receives an applied oscillating voltage (in the radio frequency range), it vibrates the crystal at the corresponding frequency forming a traveling sound wave in the crystal medium. A majority of the incident light can then scatter off the periodic sound wave peaks in a Bragg diffraction situation. This relation is given as $2\Lambda \sin \theta = m\lambda$ where Λ is the wavelength of the sound wave,

θ the angle of diffraction, λ the wavelength of light, and m the multiplicative diffraction order. In short, the driving frequency fed into the AOM determines the frequency shift of the light away from the incident light's frequency. In addition, the amplitude of the wave, which is directly proportional to the amplitude of the voltage signal, controls the diffraction efficiency, i.e. higher signal amplitude leads to more power in the diffracted beam. The cooling beams used in the MOT system are red-detuned by 14 MHz from the $F = 3$ to $F' = 4$ D2 hyperfine transition.

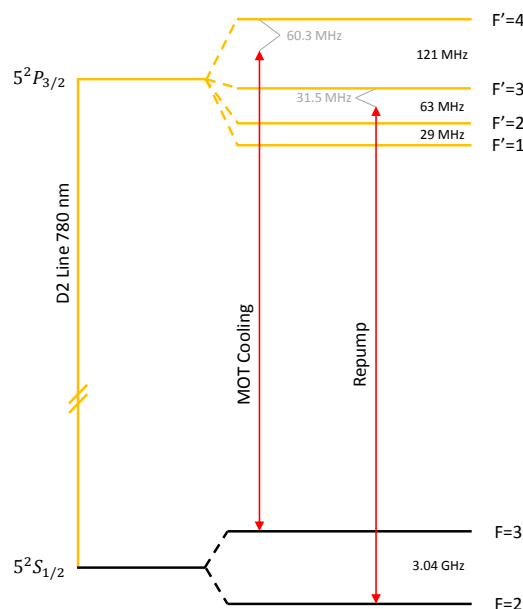


Figure 4.2: Level diagram for the ^{85}Rb D2 line in the MOT stage labeled with experimental transitions and detunings from those transitions. Note that this diagram does not include AC Stark shifts, which are factored into the experimental setup.

Repump Laser

The laser used to access the repump transition in the MOT system is also an external cavity diode laser with an optical system very similar to that of the main MOT laser. Saturated absorption spectroscopy is also used, locking this time to the crossover peak between the $F = 2$ to $F' = 2$ and $F = 2$ to $F' = 3$ D2 hyperfine lines in ^{85}RB (see Fig. 4.2). This is because the light needs to stimulate the $F = 2$ to $F' = 3$ D2 hyperfine transition in order to deplete any accumulated atomic population in the $F = 2$ state that are dark states in relation to the MOT cooling beams. An AOM is used to shift the beam's final frequency 5 MHz down (red-detuning) from the resonant peak of this transition. Geometrically, the repump beam does not need to

be oriented in a particular angle relative to the optical molasses configuration as long as it is fully incident on the location of the trapped atomic cloud.

4.2 Detection System

Observation of trapped atoms is a key component to all experimental procedures here, as it is the only basis from which to extract quantitative measurements. To detect single atoms within the microtrap, fluorescence imaging with an electron-multiplying charge coupled device (EMCCD) camera is utilized. This technique not only allows precise monitoring of the contents of the FORT, but its application consequently provides a further cooling mechanism to the trapped atoms - Sisyphus cooling, as discussed in Sec. 2.3.1. The main experiment of this thesis requires an in-trap atom counting resolution of one. The fluorescence collection from the EMCCD camera alone is not able to distinguish atom numbers between 1 and 3, and therefore a further detection method is also implemented. An approach to count single photons is used in parallel with the fluorescence collection of the camera by splitting the total light emitted by the atoms into two detection devices. Fig. 4.3 shows a diagrammatic

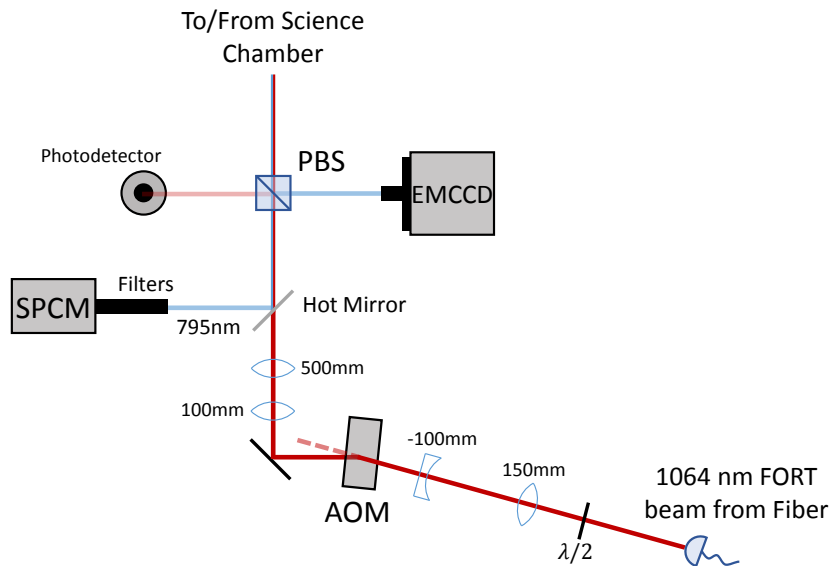


Figure 4.3: Schematic drawing of the FORT beam's entrance into the science chamber as well as the fluorescence light's exit with coupling into detection electronics. The photodetector seen here is used for constant monitoring of the FORT beam's optical power.

representation of the imaging system that is overlapped with the FORT beam. From the point of trapped atoms in the science chamber, 10% of the total fluorescence

light is collected by the high NA lens then coupled into the EMCCD camera by a polarizing beam splitter (PBS). Considering the transmission of optics (37%) and the listed quantum efficiency of the EMCCD camera (60%), the total detection efficiency of photons of this system is 2.3%. The emitted light that the PBS transmits is then directed into the single photon counting module (SPCM) by a dichroic mirror coated to allow transmission of 1064 nm (FORT) light but reflect 795 nm light, referred to as a 'hot mirror'. Before the sensitive SPCM and EMCCD camera lie optical filters to remove any stray light that may enter the beam path from the system.

4.2.1 Single Atom Imaging

The light used to prompt atomic fluorescence is linearly polarized and blue-detuned from the D1 hyperfine transition. Contrary to the D2 line, the magnetic sublevels in the D1 line manifold are not individually shifted from the AC Stark shift [23], which makes hyperfine transitions technically easier to address. Another advantage of using the D1 line is that its center frequency is nanometers away from the D2 line, making it easy to optically filter out unwanted light in certain locations. The laser's frequency is again stabilized using saturated absorption spectroscopy. While not necessary in the case of one trapped atom, the blue-detuning of the beam applies the same effect discussed in Sec. 2.5.3 - limiting of the energy gained in light-assisted collisions. This comes into play during multiple atom experiments making sure that there is very low trap loss due to detection light. Also in the vein of preventing atomic heating, the detection beam is retroreflected back into the science chamber in order to counteract any Doppler heating that may occur. Because of the retroreflection, a blue-detuned standing wave is formed, which means the atoms undergo Sisyphus cooling, as discussed in Sec. 2.3.1. This additional cooling mechanism mainly takes place on the edges of the FORT where the atomic levels are not as heavily shifted by the trap light [21].

The imaging light is detuned by 20 MHz from the $F = 2$ to $F' = 3$ D1 line. Since it addresses the $F = 2$ to $F' = 3$, excited atoms have a probability of decay to the $F = 3$ level, meaning that this is not a cyclic transition. This motivates the use of a repump beam, which can conveniently be satisfied by the six MOT cooling beams slightly detuned from the $F = 3$ to $F' = 3$ D2 transition. A schematic of the transitions used in the imaging system is seen in Fig. 4.4.

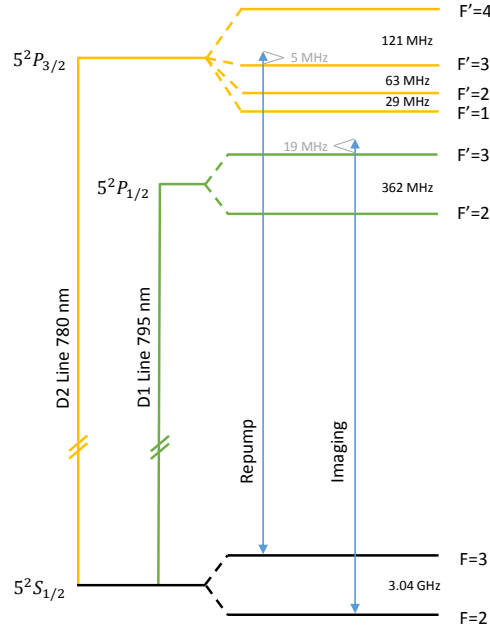


Figure 4.4: Level diagram for the ^{85}Rb D1 and D2 lines during single atom imaging labeled with experimental transitions and detunings from those transitions. Note that this diagram does not include AC Stark shifts, which are factored into the experimental setup, i.e. the detunings listed are relative to the shifted levels.

4.2.2 Counting Single Photons

When multiple atoms are present in the FORT, the presented detection scheme using the fluorescence collected by the EMCCD camera does allow for observation of them with low trap loss [68, 69]. However, the goals of this experiment mandate a detection resolution that is good enough such that the probabilities for observing signals from 1, 2, and 3 atoms can be experimentally determined. This degree of resolution is achieved when the in-trap fluorescence is collected by a single photon counting module (SPCM) alongside the EMCCD camera as seen in Fig. 4.3.

The SPCM consists of an avalanche photodiode, which is triggered by a single incident photoelectron. When a photon enters the aperture and hits the device's active area, an ejected electron exponentially amplifies an electron current by causing the negatively biased diode to become conducting. This creates a signal large enough to interpret and export a transistor-transistor logic (TTL) pulse. The pulse is read and counted by a field programmable gate array (FPGA), both of which share a timer. The FPGA then sends its count data to a computer via a LabView interface. The software packages the counts into a readable text document that lists the number of photons collected in each experiment cycle. Thus, the single atom detection is upgraded to single photon precision.

The photon count information is most effectively interpreted in histogram format. A sample histogram is presented in Fig. 4.5. Note that a detection of 0 photons corresponds to an average 'dark' count of 0.4, which serves as a calibration value. The mean values for the number of photons collected in the SPCM from emission by 0, 1, 2, and 3 atoms are distinctly separate. However, Fig. 4.5 also displays that the widths of each atom number's statistical distribution of collected photons overlap. This overlap is an experimental consequence owing to one- and two-body loss mechanisms. In the time between placement of 1, 2, or 3 atoms in the trap, initially determined by an image taken using the EMCCD camera, and a pulse of detection light to be scattered into the SPCM, one or two atoms may be lost from the trap. The two-body loss owes to the fact that the light pulse used for the SPCM is near-resonant, which means that there is a possibility of light-assisted collisions taking place. The one-body loss is discussed in Sec. 6.1. Thus, an initial atom number reading by the EMCCD camera may appear as one to three fewer atoms according to the fluorescence collected by the SPCM. Overall, the statistical distributions of photons collected from 0, 1, 2, and 3 atoms are sufficiently different to be analyzed by the curve fitting techniques described in Sec. 6.1.

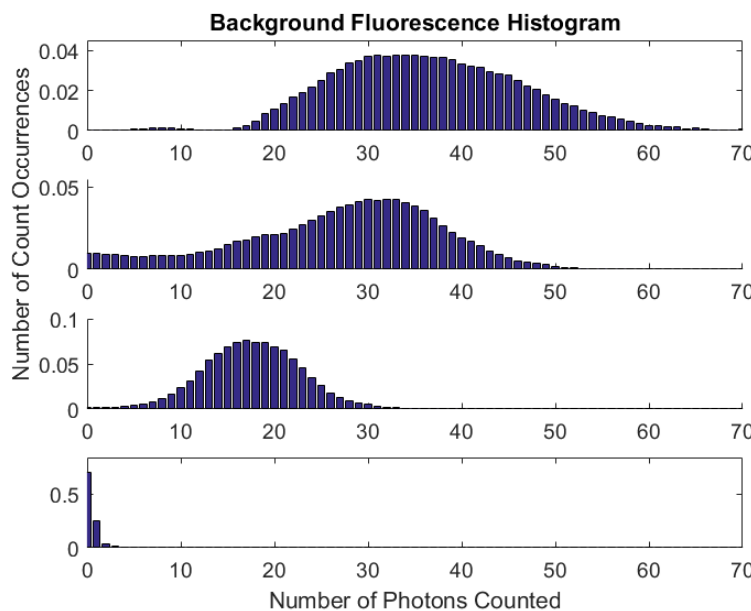


Figure 4.5: A sample calibration histogram of data collected from the SPCM. The upper plot corresponds to fluorescence collected from cases of 3 atom loading, followed underneath by instances of two, one and zero atoms respectively. The y axis signifies the number of times that the corresponding number of photons on the x were collected by the SPCM.

4.3 FORT Loading Sequence

The experimental stages necessary for single atom loading in a FORT are summarized in Fig. 4.6 including their necessary duration. These time scales were previously determined empirically. This sequence is performed during each realization of the main experiment and takes 1.4 seconds in total (0.94 s from the listed steps with and additional 0.46 s for stabilization of laser powers previous to the list). Control of the carefully timed cycle is held by a LabView interface on a 'master' computer.

The software coordinates the duration and frequency of laser pulses into the science chamber, changing magnetic fields, and position of multiple FORTS discussed in the next chapter. LabView dictates the output of analog and digital voltages from an FPGA card. The digital TTL pulses typically trigger instruments to start or stop a function such as a request to begin collection by the EMCCD camera. The analog voltage outputs allow for ramping of current to form magnetic fields as well as amplitude and frequency modulation of AOMs to manipulate various laser powers and frequencies. Each step in the string of voltage outputs has a timing precision of $2 \mu\text{s}$.

Note that the sequence listed here includes two stages not described in the above section - the compressed MOT (CMOT) and cleaning image. The CMOT's function overall is to increase the atomic cloud density and better overlap it with the focus of the FORT beam through the high NA lens, which provides more efficient atom loading of the FORT. This stage comes directly after the standard MOT formation and features a linear current ramp to an increased magnetic field

by a factor 1.45. The powers of the repump beam for the MOT and the MOT cooling beams themselves are also lowered during this phase as well as further red-detuning the beams. When the atoms are more condensed, the probability of undergoing red-detuned light-assisted collisions is increased, which would lead to increased probability of trap loss. The lower beam powers serve to offset this effect. The cleaning image stage consists of two triggers of the EMCCD camera. The first is necessary to clear the CCD register of excess thermal electrons, and the latter stores an image used to establish the background light level when processing the single atom detection images taken later in the sequence.

Stage	Duration
MOT Loading	500 ms
Ramp to CMOT	1 ms
CMOT	148.5 ms
Cleaning Image	10 ms
Light-Assisted Collisions	100 ms
Detection Image	17 ms
PGC	10 ms

Figure 4.6: Timeline of single atom loading.

5 | Implementation and Characterization of Multiple FORTs

Novel additions needed to be made to the experimental apparatus in order to accommodate three dynamic microtraps. By feeding three independent RF frequencies into the main FORT-producing AOM, seen in Fig. 4.3, three separated traps are created. Loading single atoms into each trap is performed with the previously discussed experimental sequence.

This chapter details the implementation and characterization of the multiple trap experimental setup including electronic circuitry, mapping of trap placement and movement via AOM frequency sweeping, determination of atomic temperature in the FORTs, and methods of preparing the atoms in an extreme spin polarized state. The development of the overall system was part of this thesis.

5.1 Generation of Multiple Traps

Fig. 4.3 depicts the optical system leading the 1064 nm beam, which forms the FORT(s), into the science chamber. The series of lenses that images the focus of the beam to the working distance position in front of the high NA lens translates a change in the RF frequency that drives the principal AOM, also seen in Fig. 4.3, to a change in trap position. Specifically, a change of 1 MHz in frequency corresponds to a lateral change in trap position of $0.19 \mu m$. The FORT beam's waist was measured by guiding the beam into a 100x microscope mimicking the optical system into the science chamber. Then, a Gaussian function was used to fit the intensity profile of the imaged beam in the x and y axes to find the $1/e^2$ waist, $w_0 = 1.10 \pm 0.01 \mu m$.

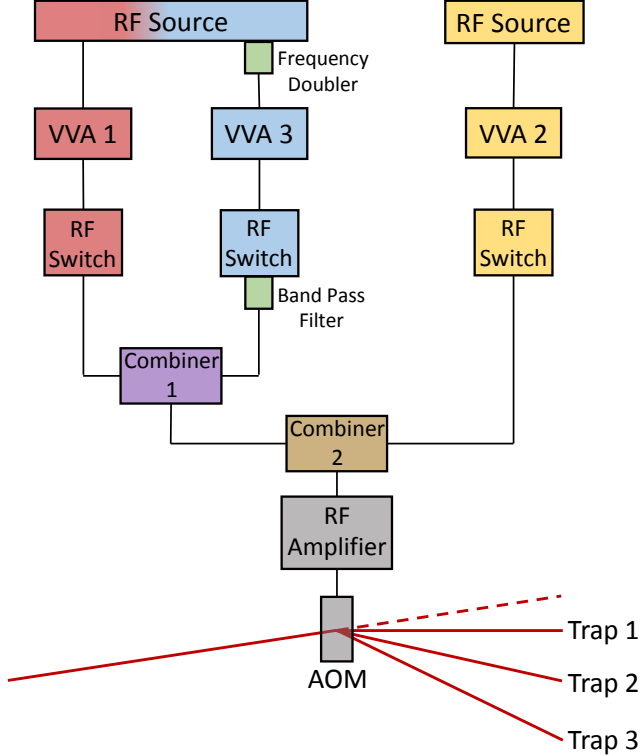


Figure 5.1: Schematic layout of RF electronics used to generate multiple FORTs via AOM deflection. Colors included to emphasize separate signal paths.

Fig. 5.1 shows a schematic representation of the network of RF electronics used to gain independent control of each FORT. Two frequency generators begin the chain outputting initial frequencies of 88.5 MHz, 112.5 MHz, and 136.5 MHz, which are referred to as traps 1, 2, and 3 respectively. When these frequencies are fed into the AOM, three separate first order diffraction beams, whose angle depends on the frequency, emerge as shown in Fig. 5.1. Note that the output used for trap 3 must be doubled out of the source due to constraints of the instrument. The analog voltage outputs from the master computer control system (see Sec. 4.3), are utilized to control the amplitude of each RF frequency sent to the AOM. Recall that this in turn dictates the amount of optical power that the AOM deflects. A user-specified voltage from the computer is received by a variable voltage attenuator (VVA) for each frequency. This circuit element dynamically adjusts the source signal's amplitude from the frequency generator. Next, each signal passes through a simple RF switch that either transmits or suppresses the now attenuated signal, which translates to abruptly turning a trap on or off. Each switch is controlled by a digital TTL pulse from the master computer. A band pass filter after the switch in trap 3's signal path mitigates the effects of sidebands created by the frequency doubling unit.

Because trap 2 is taken to be stationary and central, the signal paths for traps 1 and 3 are grouped together in the circuit for convenience of debugging. Using an RF combiner element, the signals used for traps 1 and 3 are added together followed by an addition of trap 2. Because the frequencies are relatively close together in value, noticeable interference effects come into play at substantial signal amplitudes. This is why each of the signals are added together then amplified. The RF amplifier increases each signal by a gain factor of 40 dB. With this multiplier in mind, the total RF power fed into the AOM cannot exceed its damage threshold of 1.5 W average power, which functionally limits the possible transmitted optical power into each trap beam. That means careful attention must be paid to the levels of each trap's signal power ultimately set by the master computer.

In order to maintain stable RF signals into the AOM and avoid undesirable heating effects on the atoms, the circuit shown in Fig. 5.2 was installed to control the AOM in Fig. 4.3 and in turn, the power of the FORT beam. Consider an unstable RF signal used to drive the AOM - meaning an inclusion of some non-negligible noise or a drift in total power on a relevant timescale. That would equate to a deflected beam whose optical power holds the same instability. In the experimental scenario, that deflected beam is focused and used as a FORT to hold a single atom. Recall from Sec. 2.4 that the potential created from the dipole interaction is proportional to the incident light's intensity. In other words, the power of the beam corresponds to the depth of the potential well seen by the atom. If that depth is constantly changing due to such an electronic instability, then the atom is heated due to the gained kinetic energy from the 'shaking.' Excess heating of the atom can lead to its exit from the trap, and therefore is unwanted experimentally.

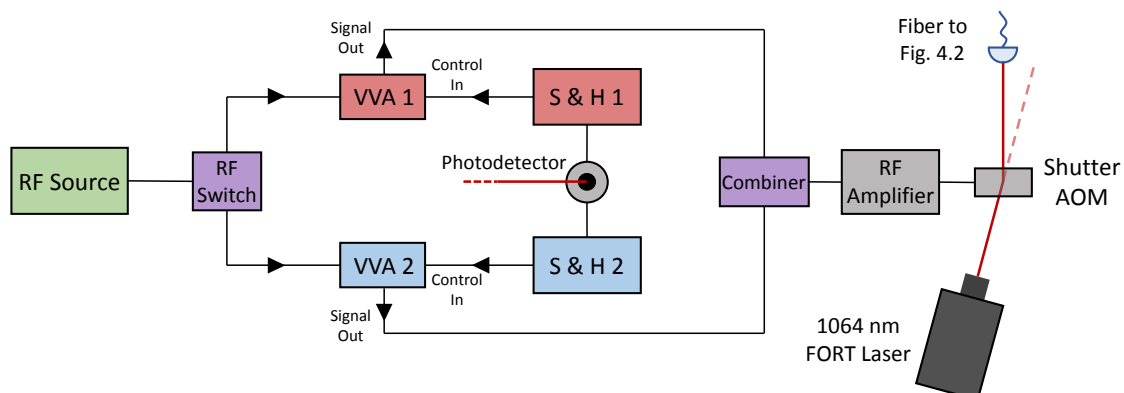


Figure 5.2: Schematic layout of RF electronics used to actively stabilize the optical power of each FORT beam. Colors used to emphasize signal path separation.

After the FORT laser beam leaves its source, it first passes through an AOM referred to as a shutter. Its first order deflection is aligned to an optical fiber that carries it to the series of optics leading to the science chamber, seen in Fig. 4.3. Thus, a beam is only delivered to the chamber when the shutter AOM is driven. The overall optical power used for the multiple traps can be controlled and stabilized at this point. Following Fig. 5.2, an 80 MHz RF signal exits the frequency generator and passes through one arm of an RF switch. The switch is triggered by a TTL pulse from the master computer and ultimately allows for power stabilization on one of two possible levels. The two levels correspond to a 'deep' potential well and single atom loading stage potential depth, later seen in Fig. 5.9 and discussed in Sec. 5.5.1.

Each arm of the RF switch leads to a VVA (labeled 1 and 2 to emphasize signal path separation) where the signal's amplitude can be precisely adjusted. The photodetector, also seen in Fig. 4.3, that is used to monitor the amount of optical power sent into the science chamber gives this voltage value to two custom integrator circuits labeled S & H 1/2. S & H stand for 'sample and hold' referring to the fact that the circuit actively reads a signal from the photodetector, and adjusts its output value to match a user-set level via a standard integrator circuit. 'Sample' mode means the device is performing active amplitude stabilization, and 'hold' mode means that stabilization feedback is ignored so that the FORT beam's power can be dynamically adjusted. By controlling each VVA with this active stabilization scheme, the amplitude of the RF signal driving the shutter AOM (Figs. 4.3 and 5.2) is actively stabilizing, thereby fixing the optical power sent through the main AOM (Fig. 5.1) creating one or multiple FORTs.

5.2 Mapping of Trap Positions

5.2.1 Static Trap Positions

The three traps have distinct positions in space, again, dictated by the driving RF frequency fed into the principal AOM. The beam waist of each is assumed to be $1.10 \pm 0.01 \mu m$ (this value was previously measured for the central trap frequency, trap 2, and is assumed to be the same for traps 1 and 3 even though they likely experience some aberration due to their slightly off-center transmission through the high NA lens). There are two main experimental phases to consider: single atom loading and trap merging. To merge the potential wells felt by each atom, the driving

RF frequencies for traps 1 and 3 are swept by the function generator ('RF Source' in Fig. 5.1) so that the FORT beams overlap.

The spatial distances between the traps during the loading phase were determined empirically. If they are too close, the atoms in each trap have a nonzero probability of hopping to the adjacent trap [70]. In addition, the combined RF signals see increased interference effects when their frequency separations are decreased, which means the potential wells are perturbed more. These factors suggest that a wide trap spacing during single atom loading is advantageous for system stability. The limiting factor in trap separation is available optical power. Because the FORT beam passes through an optical fiber before it is separated into multiple beams, the maximum power incident on the fiber is ~ 2 W to prevent damage to the fiber tip. Furthermore, any AOM has an optimal range of operating frequencies determined by the properties of its crystal and RF electronics. This means that the further the driving frequency from the optimum value, the less optical power it deflects into each order at maximum driving amplitude. The depth of each trap during single atom loading and detection is $h \times 57$ MHz, which is a set to match necessary detunings from resonance according to the AC Stark shifted energy levels. With this condition, I found a static trap separation of $4.5 \mu\text{m}$ (24 MHz frequency separation) to be the maximum, and thus optimum value. Thus, single atom loading was performed at this trap separation. The actual frequencies of the AOM driving signals are 88.5 MHz, 112.5 MHz, and 136.5 MHz for traps 1, 2, and 3 respectively. The minimum trap separation required to mitigate undesirable effects (trap loss, atomic heating, etc.) during single atom loading was $2.7 \mu\text{m}$ (15 MHz frequency separation). An example picture of three atoms confined in the static traps as seen by the EMCCD camera is shown in Fig. 5.3.

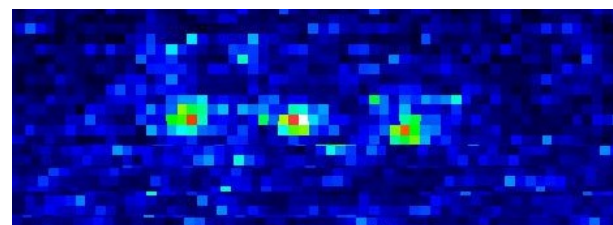


Figure 5.3: Example picture of three separated ^{85}Rb atoms in confined in static traps as seen by the EMCCD camera. False color plotting is used to show relative fluorescence levels.

5.2.2 Merging Potentials

Starting from their static positions for loading, the frequencies of the AOM driving signals for traps 1 and 3 are linearly swept by a built-in function of the function generator in order to merge all potentials into one. Once they are combined, traps 1 and 3 are slowly turned off by linearly ramping their driving amplitudes to zero. The necessary trap separation when considering the potentials as merged is $0.85 \mu\text{m}$ (4.5 MHz frequency separation). This was found empirically to be the widest separation in which trap-to-trap transfer could be performed with an atom retention of 100%. Again, a wider separation leads to less amplitude modulation from interference. When the driving frequencies are close for merging, the modulation is fast compared to the atomic motion, and the atoms feel a time-averaged potential. With this in mind, the sweeping and merging of traps was performed at shallow trap depths of $h \times 7.3 \text{ MHz}$.

To sustain a controllable experimental setting, bringing the isolated and cooled atoms from their static positions into a single potential well where they are allowed to interact must be done in a near-adiabatic fashion. Specifically, adiabaticity is achieved in this situation when the duration of trap movement is much greater than the order of the oscillation period of the trapped atom. The atom's oscillation frequency is calculated by first approximating the FORT to form a Gaussian potential,

$$U(r, z) \approx -U_0 \left(1 - \frac{2r^2}{w_0^2} - \frac{z^2}{z_R^2} \right) \quad (5.1)$$

where w_0 is the laser beam waist, U_0 is a constant offset, and z_R is the Rayleigh length, $z_R = \frac{\pi w_0^2}{\lambda}$. Then, compare the radial and axial terms to the classical potential for a harmonic oscillator. Thus,

$$\omega_{radial} = \sqrt{\frac{4U_0}{w_0 m}} \quad \text{and} \quad \omega_{axial} = \sqrt{\frac{2U_0}{z_R m}} \quad (5.2)$$

for the mass of the atom, m . For the shallow trap depth used for sweeping and merging, $h \times 7.3 \text{ MHz}$, the oscillation frequencies of the ^{85}Rb atom are 53 kHz in the radial dimension and 11 kHz in the axial dimension. Under consideration of these frequencies, a trap sweeping time of 40 ms was found to be sufficient.

Moreover, when the potential wells coalesce, they must be the same depth to avoid any 'pouring' effects, as shown diagrammatically in Fig. 5.4, and maintain near-adiabaticity when transferring atoms. Suppose one of the outer dynamic traps

has a potential well depth that is shallower than the central static well by some potential energy, Δ . Then when traps are merged, the outer atom will fall into the middle trap and gain a proportional amount of kinetic energy. Therefore, $\Delta \rightarrow 0$ is the condition for adiabaticity in this aspect when merging. The balance of trap depths is complicated by including the deflection efficiency curve from the multi-trap AOM. When the trap-forming signals are swept together in frequency to merge, their amplitudes must be dynamically corrected to stay at the same level through the sweeping process. That is achieved by linearly ramping down the voltage control into VVA 1 and 3 in Fig. 5.1 (with S & H boxes in 'hold' mode) to offset an increased deflection efficiency when moving toward the more efficient central frequency of trap 2.

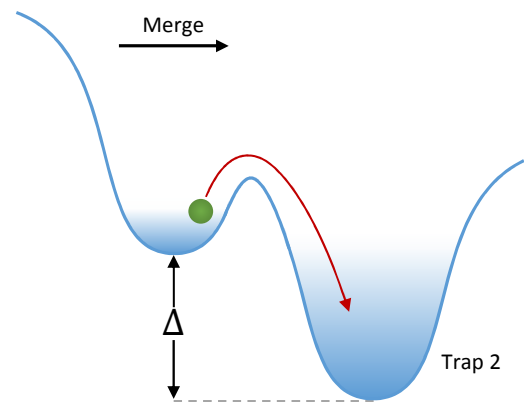


Figure 5.4: Diagram of trap 'pouring' in the merging process. When the depths of the traps differ by some amount Δ , the transferred atom gains a similar amount of kinetic energy.

5.3 Assessment of Single Atom Temperature

Knowledge of the temperature of the individual atoms while trapped is imperative for understanding the efficacy of our cooling schemes, calculating the three-atom 'cloud' density, and demonstrating near-adiabaticity when moving the traps. To measure the atom temperature, a method of 'release and recapture' (RR) is employed [71]. To perform this experimental technique, a single atom in one trap is first detected with the EMCCD camera. Then, the trap depth is lowered adiabatically - done by ramping its optical power in 10 ms - to $h \times 7.3$ MHz. The RR measurement is taken when the atom is then *released* by turning off the FORT light for some variable duration, Δt , allowing it to freely expand, then *recapturing* it by turning the trapping

light on again. The trap depth is ramped back up to its standard operating value, and a second detection image is taken to find out if the atom survived the RR process. This sequence is repeated 100 times for all release times, Δt . Fig. 5.5 shows an example plot of survival probability versus release time. Note that RR must be performed at a shallow trap depth, as it is not accurate at higher trap potentials in this FORT. This is likely due to nonlinear heating of the FORT optics when substantial power is used leading to a small discrepancy in beam position when the light is applied to recapture the atom. This would imply that more atoms would fail to be recaptured, causing an overestimation of the temperature, T .

To obtain the temperature, T , from this plot, a Monte Carlo simulation is performed and fit to the data. The analysis program was originally written by former postdoctoral fellow, Dr. Andrew Hilliard. In this simulation, a thermal (Maxwell-Boltzmann) distribution for some temperature, T , is set to randomly generate an initial atom position and momentum. Then, the atom's velocity and position are calculated after a free expansion time, Δt . The simulation program determines an atom to survive the RR process if its calculated final kinetic energy is less than the depth of the potential well formed by the FORT. The atom retention probability calculation is iterated 5000 times for each release time, Δt . Finally, the calculated points are fit to the experimental data with a least squares fitting method.

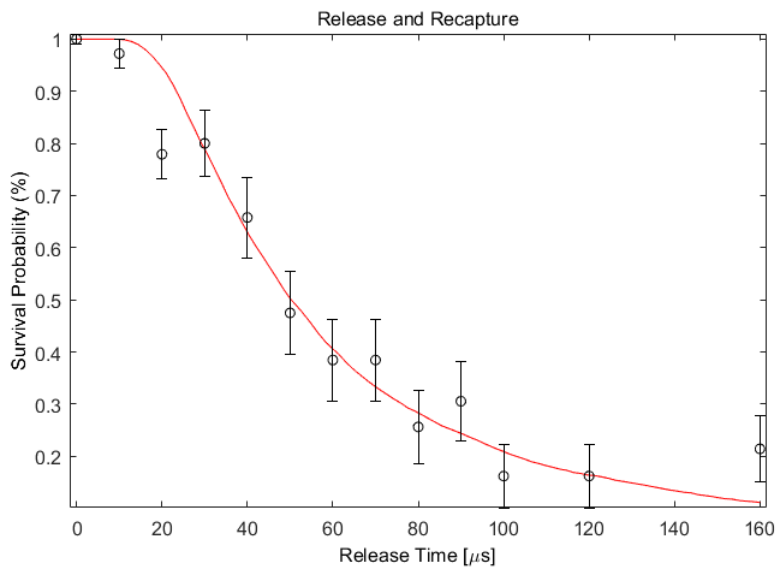


Figure 5.5: Determination of atom temperature through release and recapture process. **Black** circles indicate measured data, and **red** line is the fit curve from Monte Carlo simulation. Best fit temperature = $7.7 \pm 0.4 \mu K$ at trap depth = $h \times 7.3 \text{ MHz}$.

Measuring atomic temperature in this manner is suitable to demonstrate that the sweeping and transfer of atoms from the outer dynamic traps 1 and 3 to the central static trap 2 is near-adiabatic. First, the temperature of a single atom that has been loaded and cooled in trap 2 is measured to be $8.0 \pm 0.4\mu K$. This serves as the comparison value for the swept traps, as it is the baseline value of a static trap. Next, release and recapture was performed on an atom that was loaded into trap 1, as detected by an imaging pulse, cooled through PGC, then swept and transferred into trap 2; the measured temperature was $13.3 \pm 0.9\mu K$. Similarly, the temperature of an atom transferred from trap 3 to trap 2 was $7.0 \pm 0.5\mu K$. The apparent discrepancies in these measurements is relatively inevitable. Even though the determination of atomic temperature is performed under the same circumstances - RR on a cooled atom in trap 2 - the systemic details of their preparation are slightly different. Precise knowledge of the atom's thermal status is unknown before its transfer to the central trap for measurement, and a minor difference in trap depth than initially measured via optical power meter ultimately leads to different cooling parameters (the AC Stark shifted levels are moved). Therefore, it is difficult to asses the true atomic temperature because of subtle uncontrollable variations in the experimental method. Overall, the measured temperatures of atoms coming from swept traps are comparable to that of atoms in the static trap, which implies near-adiabaticity for the merging process.

When the three atoms are mixed into the same potential well, the ensemble temperature is taken to be the average of their individually measured temperatures, $9.4 \pm 0.4\mu K$. This assumes that the three bodies thermalize through elastic collisions, and there is a tendency toward a state of equipartition of energy in the system [72].

5.4 Preparation of Extreme Spin Polarized Atomic States

The focus of this experiment lies on inelastic collisions between identical bosons. When indistinguishable particles interact, whether fermions or bosons, a strictly quantum mechanical effect arises, known as the exchange interaction. Because particle identity cannot be discerned in such a multi-particle system, switching particle indices (labels) when calculating any expectation values in a quantum system must be done with no effect to the system. This leads to the symmetrization postulate, which mandates that a system of two or more identical particles be either symmetric or antisymmetric under the exchange of any two particle indices [22]. Bosons are required to maintain overall symmetric states, while fermions keep antisymmetric states. If a quantum state is symmetric, its state vector remains unchanged under

the exchange operation, i.e. switching two particle indices, whereas antisymmetric states acquire a phase shift under this operation.

Consequently, the exchange interaction in fermions leads to the well-known Pauli exclusion principle, stating that two fermions cannot occupy the same spatial state and spin state. That would imply an overall symmetric wavefunction. More relevant here is the nature of bosons in reaction to this phenomenon. When assessing the distribution of expectation values for interparticle separation, centered around the coordinate system's origin for example, the peak density lies at exactly at zero for symmetric states [22]. This implies that identical bosons are more likely to be found in the same location than the same distinguishable bosons would be. In this experimental scenario, the fictitious 'exchange force' discussed here thus promotes a higher likelihood for atomic collisions to occur. Indistinguishably of the single atom states is therefore advantageous to observe a clearer loss signal due to inelastic collisions. In this experiment, all three separate atoms are prepared in their extreme m_F ground state, namely $|F, m_F\rangle = |2, -2\rangle$ before they are allowed to interact.

Experimental Realization

To produce atoms only in the extreme spin polarized state, selection rules for hyperfine transitions are utilized in an optical pumping scheme. The possible optical transitions in this situation are depicted in Fig. 5.6. By exposing the atoms to a pulse of σ_- light resonant with the $F = 2$ to $F' = 2$ D1 transition (blue arrows in Fig. 5.6), the atoms can only undergo transitions in which $\Delta m_F = -1$. Although, during spontaneous emission (red arrows in Fig. 5.6), the output photon has random polarization and can relax to the $m_F = 0, \pm 1$ sublevels of the $F = 3$ or $F = 2$ ground state. This motivates the use of the six MOT cooling beams as a repump back into the $F = 2$ state, seen as green arrows in Fig. 5.6. Once the transitioning atoms have reached the outer $m_F = -2$ state, they become 'dark' to the incident σ_- light, i.e. there are no arrows leaving this sublevel, thus accumulating in that state in a small pumping time. Note that in order to deliver the optical pumping light to the atoms, the quantization axis of the atoms needed to be changed from the FORT beam's axis and redefined to match the path of the optical pumping beam due to geometrical constraints of the experiment. This applied magnetic field has the value, $B = 7.50 \pm 0.01$ G.

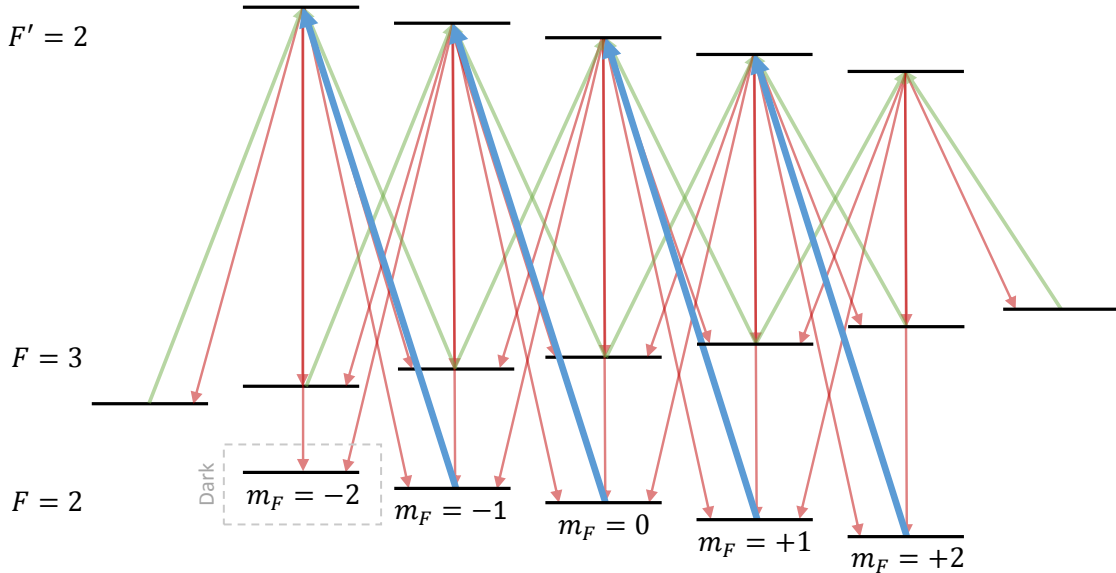
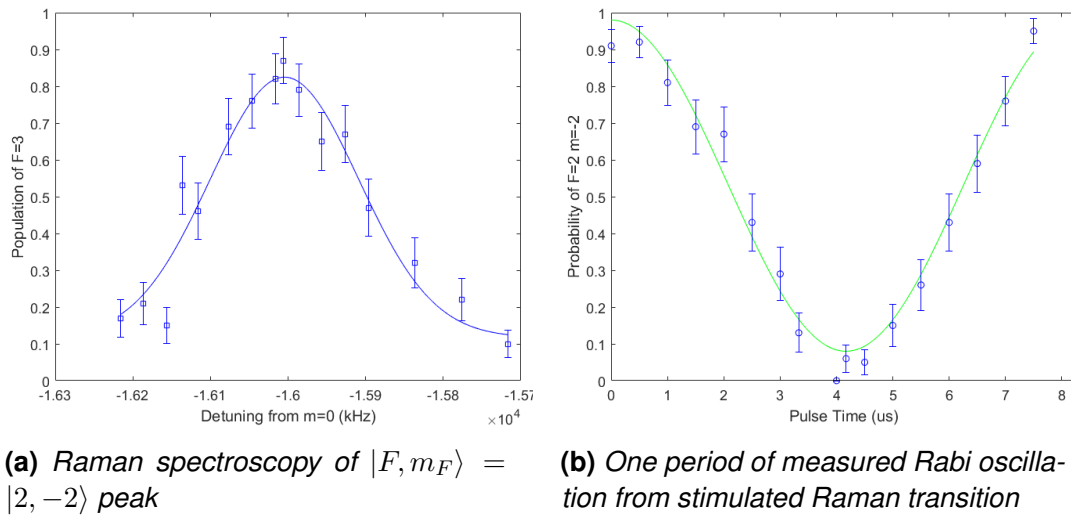


Figure 5.6: Diagram of the extreme spin-polarized optical pumping technique. Atoms in the $F = 2$ ground state are stimulated to the $F' = 2$ excited state with σ_- light (**blue arrows**). Atoms that have relaxed through spontaneous emission (**red arrows**) to the $F = 3$ ground state are repumped back to $F = 2$ using the MOT cooling beams of all polarizations (**green arrows**). Population accumulation must occur in the dark $|F' = 2, m_F = -2\rangle$ state. Zeeman shifts are included but not to scale.

If the polarization of the optical pumping light is not purely circular polarized in the σ_- orientation, then there will be small population of atoms accumulating in the rest of the m_F state manifold. This contamination would be a substantial source of experimental uncertainty in the three-body collision experiment. To test the efficacy of the optical pumping light, I utilize a stimulated two-photon Raman transition along with the push-out technique [73]. First, the optical pumping light is applied to a trapped atom (along with repump light), which should put it into the $|F, m_F\rangle = |2, -2\rangle$ state. Then, a pulse of two copropagating beams stimulates a two photon Raman transition to transfer the population into the $|3, -2\rangle$ state. Delivery of a push beam follows, which ejects any atoms in the $F = 3$ state. Finally, a detection image is taken. If the atoms were truly prepared in the extreme m_F state, they would be pushed out of the trap and not detected, provided the population transfer via Raman transition is efficient.

Experimentally, the Raman lasers first need to be tuned to be resonant with the $|2, -2\rangle$ state rather than some other m_F state. Scanning the frequency difference between two co-propagating Raman beams by means of another AOM in reference to the position of the $m_F = 0$ peak yields the resonance curve in Fig. 5.7a. The frequency difference is ultimately set to match the peak position. Next, the Raman

**Figure 5.7**

pulse duration is varied. Because this system has essentially been reduced to two levels ($|2, -2\rangle$ and $|3, -2\rangle$), the populations of each state follow a Rabi oscillation pattern, as seen in Fig. 5.7b. The most efficient population transfer, judged by the most complete depletion of the $|2, -2\rangle$ state, occurs for a pulse duration that at the valley of this curve, referred to as a π -pulse. The duration of the Raman pulse is then set to match the π -pulse time found from the fit data.

After the Raman transfer beams are tuned, the optical pumping is tested. First, the duration of optical pumping light is varied while monitoring the percentage of atoms that survive the push-out process. The characteristic time of this decay curve is labeled the pump-in time, τ_{in} , as it signifies the rate of accumulation in the $|2, -2\rangle$ state. This measurement is seen in Fig. 5.8a. Finally, a survival measurement is taken with the Raman pulse removed, and the atom is exposed to two pulses of optical pumping light followed by an exposure to light used for the push-out state detection. The first pulse is long enough to pump the atom population into the dark $|2, -2\rangle$ state, as determined by the pump-in measurement. For the second pulse, no repump beam is applied to the atoms. Optical polarizations in the laboratory setting always have some small degree of contamination from their prepared orientation. Then the optical pumping light that was used to drive transitions into the dark state using σ_- light, will also drive them out due to a small amount of alternate polarization in the light. The population that gets driven out of the $|2, -2\rangle$ state during the second pulse will end up in the $F = 3$ state because there is no repump transition available. The push-out beam then ejects any atoms pumped out of the $|2, -2\rangle$ state. Additional

exposure time for the second pulse of optical pumping light means additional atoms will be ejected. The characteristic time of decay of the trap population here is labeled the pump-out time, τ_{out} , and the experimental curve is seen in Fig. 5.8b.

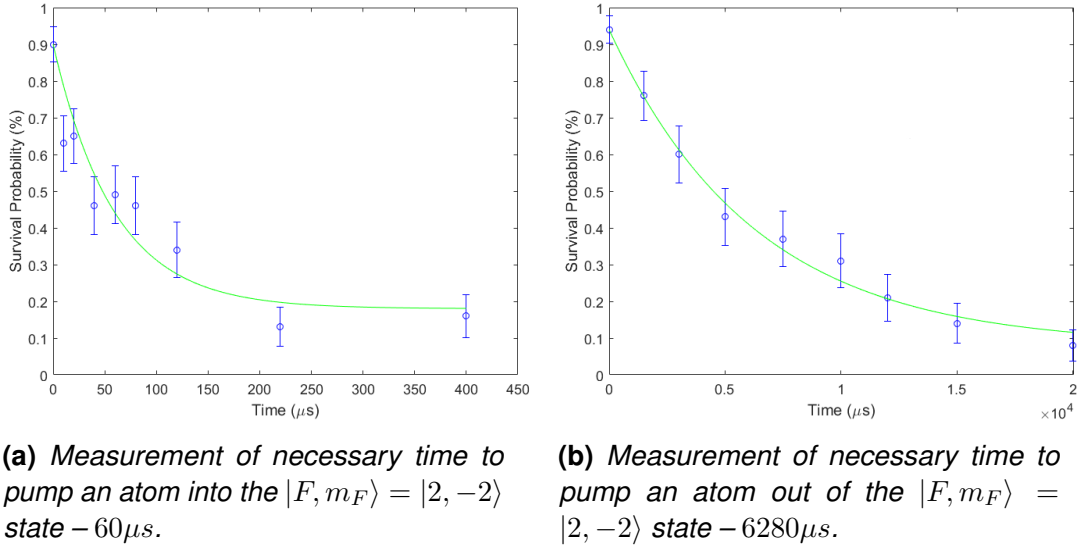


Figure 5.8

The overall efficiency of the optical pumping process is then calculated in the steady state by a scaled difference of pump-in and pump-out rates, $1 - \tau_{in}/\tau_{out}$. That means, the optical pumping efficiency for this experiment is 99.1%, implying that atoms exposed to the optical pumping light are indeed transferred to the $|2, -2\rangle$ state near-deterministically.

5.5 Measurement Methods of Few-Body Collisions

The experimental goal of this thesis is to observe three-body inelastic collisions between ultracold ^{85}Rb atoms in a FORT and measure the rate at which they occur. To do this, three separate single atoms are prepared in a specific state and combined in the same potential well. Because inelastic collisions convert enough internal atomic energy to kinetic energy for them to exit the trapping potential, an observation of trap loss corresponds to an observation of a collision event. By increasing the depth of this well, the density of the atom ‘cloud’ increases, the atoms have a greater chance of collision, and the collision rate increases. A schematic diagram of the experimental timeline is seen in Fig. 5.9 and is the subject of this section.

5.5.1 Experimental Sequence

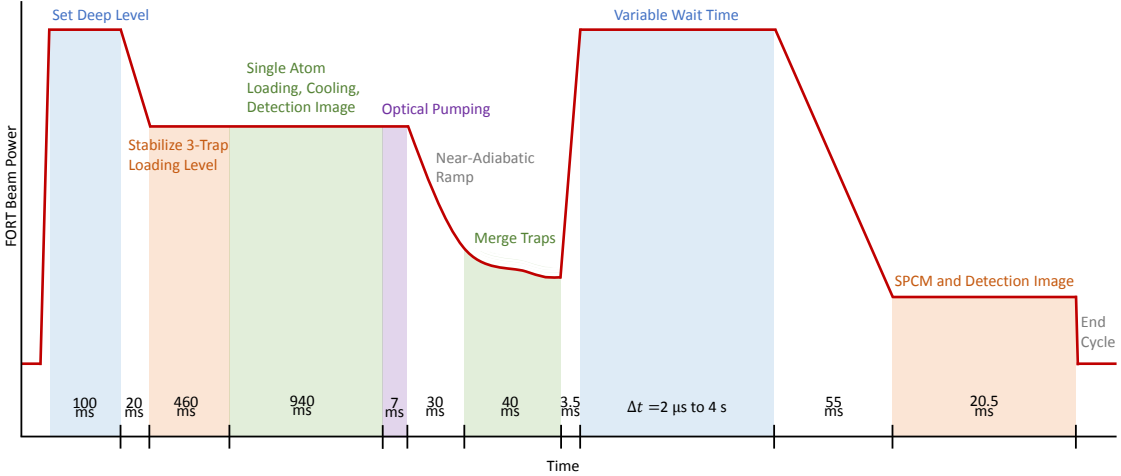


Figure 5.9: Diagrammatic timeline of experiment to measure three-body inelastic collision rate as read by power output in the FORT beam.

Each repetition of the experiment cycle begins with the establishment and stabilization of all laser powers. First, the level of FORT laser power necessary to create the particular merged atom potential depth is set and briefly stabilized using arm 1 in Fig. 5.2. Initially setting this power level allows for a seamless transition back to it later in the sequence. 100 ms is a liberal period for this task. Next, control in Fig. 5.2 is switched to control arm 2, and the overall power level needed to create three FORTS, each with a depth of $h \times 57 \text{ MHz}$, is set and actively stabilized. During this 460 ms period, assignment of powers used for the optical molasses, repump, and detection imaging lasers also occurs via the same 'sample and hold' scheme as in the FORT laser case. The following 940 ms is used to load, cool, and detect the three separated atoms as discussed in Sec. 4.3. An optical pumping pulse is then applied. The pulse duration is chosen to be 2 ms, as it is safely above the characteristic pump-in time, but well under the characteristic pump-out time (see Fig. 5.8). That means the $|F, m_F\rangle = |2, -2\rangle$ should be fully populated and relatively unaffected by slight polarization contamination.

After the atoms are isolated in static traps and prepared in the extreme m_F state, the inelastic collision experiment begins. First, the depth of each trap is slowly lowered to their merging level, $h \times 7.3 \text{ MHz}$. 30 ms was found to be sufficient to keep the near-adiabaticity of the sweeping process. After that, the merging process described in 5.2.2 takes place, in which the three atoms are consolidated into one trap while the outer two dynamic traps are ramped off. The single potential is then

amplitude-ramped to the 'deep' trap level in a duration just long enough to not invoke any atom loss or excess heating. Ideally, this would be done instantaneously in order to keep the interacting atoms at a homogeneous potential depth, but any time shorter than the selected duration was found to cause significant heating. The 'deep' trap depths used in 4 trials of the experiment were $h \times 160$ MHz, 203 MHz, 246 MHz, and 290 MHz. In each of these sets of data collection, the interaction period spent by the atoms in the deep potential, labeled the 'wait time,' is taken to be an independent variable. Depending on the depth, 9 characteristic times were selected. These can be seen in the results plotted in Fig. 6.1. The power of the FORT beam is actively stabilized for the entirety of the wait time, again using arm control 1 in Fig. 5.2.

After the atoms are placed in a regulated interaction scenario, detection of remaining atoms takes place to measure one- to three-body trap loss. A downward ramp of trap depth to $h \times 57$ MHz precedes this for 5 ms. However, during this time a mechanical shutter used to block any possible light going into the science chamber in the path of the optical molasses beams must reopen, so that these beams can act as a repump in the detection phase. This mechanical shutter lies near the source laser, and its opening sends a small mechanical vibration through the optical table, slightly shaking the laser itself. More specifically, the optical mount holding the grating which controls the frequency output of the laser can vibrate. Therefore, the frequency of the repump light used in the detection process is unstable directly after the mechanical shutter opens. An extra period of 50 ms was allotted as relaxation time for the grating mount allowing the repump laser's frequency to restabilize. 50 ms was found to be the shortest possible time that does not alter the level of fluorescence detected by the SPCM. In total, the downward ramp phase including laser stabilization time is 55 ms. To end the experiment, a 3.5 ms SPCM pulse is applied to the atom(s) followed by an additional 17 ms detection pulse collected by the EMCCD camera. A 3.5 ms fluorescence-inducing pulse for the SPCM stage was found to be optimal in order to maximize the separations of fluorescence distributions while limiting two-body loss from increased exposure to near-resonant light.

6 | Results of Atomic Loss

Observing three-body dynamics on the scale of three atoms is unique to ultracold atomic physics. In prior experiments, the rates of two- and three-body inelastic collisions have been extracted from overall population loss from an ensemble of atoms in a BEC. The many-body experimental strategy leads to a more approximate model of the changing density profile of the atom cloud, and it presents a challenging separation of contributions from two- and three-body trap loss processes [7, 66]. Until the experiment in this thesis, there has not been a measurement of three-atom collision dynamics performed with three individual atoms.

Here, I present the results of a direct measurement of three-body recombination in ^{85}Rb . By loading three isolated atoms prepared in the same quantum state into independent FORTs and near-adiabatically merging them into the same potential well using the previously described apparatus, three-body trap loss due to energy gained from inelastic collisions was measured. Comparison of these results to established theory shows good agreement and is also discussed in this chapter.

6.1 Measurements of Three-Atom Collisions

Because the loading of each of the three FORTs has an efficiency under unity, the experimental sequence detailed in Section 5.5 needed to be repeated many times to gather sufficient statistics from which to draw valid conclusions. Only instances in which single atom loading occurred in all three traps are of interest. The first detection image of the experimental sequence allowed for the selection of these instances out from the rest of the experimental repetitions. Cases of one, two, and zero atoms loaded into the FORTs were also sorted according to the results of the first detection pulse in the EMCCD camera. Three-atom loading accounted for 35.67% of experimental realizations. This corresponds to an average single trap loading efficiency of 70.9%.

Once the single atoms were loaded into each FORT, they did not all survive the experimental process due to other reasons than three-body inelastic collisions. When only one atom in total was loaded, as indicated by the first detection image, it was found to survive the merging and trap depth ramping processes 94% of time. The main reasons why this number is not unity, are the single atom detection efficiency, $\sim 98\%$, and the finite single atom trap lifetime due to experimental limiting factors like the vacuum lifetime.

Although this is not a major source of systematic error, it warranted consideration when calibrating the histogram sets collected with zero added wait time - example seen in Fig. 4.5. The histograms with zero added wait time, labeled \tilde{H} , were used to set the standard for fluorescence levels and distributions for cases of 0 – 3 atoms loaded, histograms labeled H_0 – H_3 respectively, when wait time was added to the sequence. Thus, these needed to be calibrated such that trap loss due to only inelastic collisions would be assessed.

To correct the accumulated sets of \tilde{H} , the 'zero atom' range of photon counts appearing in H_1 were first removed. There was a clear separation in that case between fluorescence distributions, the mean of $H_0 \approx 0.4$ and the mean of $H_1 \approx 17$. Then, H_1 was normalized to the area of the one-atom fluorescence distribution. Next, the amplitude of H_2 was lowered by a factor of $(1 - 0.94^2 - 0.06^2)$ to represent the combinatorial chances of one-atom loss. H_2 was then normalized to its distribution area. Finally, H_3 was decreased by a factor of $3(1 - 0.94)^3$, accounting again for the probability of single atom loss in the scenario of three-atom loading. With these corrections, the fluorescence distributions in \tilde{H} could serve as accurate baseline atom loss measurements.

6.1.1 Atom-Loss Rates

Three-body loss rate data were collected at various 'deep' trap levels during the period in which the atoms were allowed to interact. By altering the time of the interaction duration, or wait time, a functional form of the trap loss due to one-, two-, and three-body inelastic collisions could be plotted. Ten characteristic wait times were chosen for each trap depth: $h \times 160$ MHz, 203 MHz, 246 MHz, and 290 MHz, and at least 600 experimental realizations were performed at each wait time. After the initial atom number (0 – 3 in separated traps) was established by results read from the EMCCD camera from the first detection image and sorted to only analyze the instances of three atoms loaded, the final atom number left in the merged trap

was counted by the SPCM in histogram form. These histograms were analyzed with calibration according to the fluorescence collected when no additional wait time was included as described in the previous section. The fraction of instances for each atom number counted by the SPCM is plotted against wait time in Figs. 6.1a - 6.1d. Note that the horizontal axes of these plots, 'wait time (sec.)' are scaled differently according to the data range. The data points were fitted with the set of solutions listed in Eq. 3.43 (see also Appendix A) using MATLAB's nonlinear curve fitting package. The rates of three-body loss, γ_3 , are presented in Table 6.1.

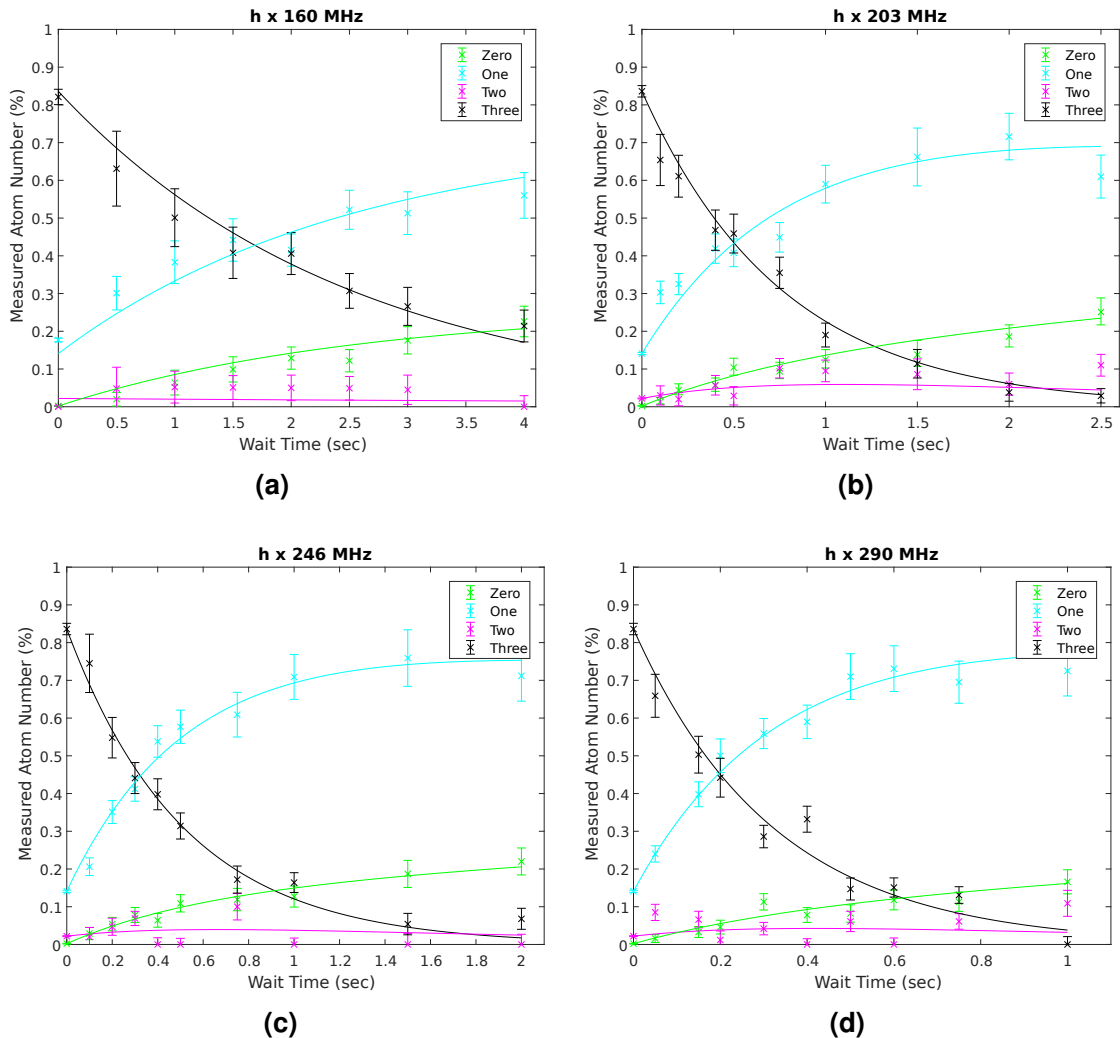


Figure 6.1: In-trap atom population determined by the SPCM fluorescence measurements plotted against interaction duration - termed 'wait time'. Note that the 'deep' trap level in which each experiment took place is listed at the top of the plots, and that the horizontal axes are scaled according to the range of data.

6.1.2 Atomic Density

In order to convert the experimental loss rates, γ_3 , into comparable experimental values for the three-body recombination rate, K_3^{exp} , the density profile of the three trapped atoms first needed to be determined. Then, K_3^{exp} could be calculated using a relation simplified from Eq. 3.39,

$$\gamma_3 = K_3^{exp} \int_{\text{All space}} n^3(\mathbf{r}) d\mathbf{r}^3 \quad (6.1)$$

where $n(\mathbf{r})$ is atomic density normalized to atom number, $N = 3$, and \mathbf{r} is a general spatial coordinate. Considering the Gaussian potential formed by the FORT in Eq. 5.1, a thermal distribution of atoms is assumed for the density profile,

$$n(\mathbf{r}) = n_0 \exp\left(\frac{-(U(\mathbf{r}) + U_0)}{k_B T}\right) \quad (6.2)$$

Then the simplified density function is,

$$n(\mathbf{r}) = n_0 \exp\left(\frac{-2U_0x^2}{k_B T w_0^2}\right) \exp\left(\frac{-2U_0y^2}{k_B T w_0^2}\right) \exp\left(\frac{-U_0z^2}{k_B T z_R^2}\right) \quad (6.3)$$

where n_0 is a normalization constant set by the condition $\int_{\text{All space}} n(\mathbf{r}) d\mathbf{r} = N = 3$. The atom number normalization allows K_3^{exp} to track three-atom loss events. The peak densities calculated for each trap depth are listed in Table 6.1. Using this form

Trap Depth		γ_3 (1/sec)	Peak Density, n (cm ⁻³)	K_3^{exp} (cm ⁻⁶ /sec)
(Frequency)	(Temperature)			
$h \times 160$ MHz	$k_B \times 7.7$ mK	0.12 ± 0.01	$(5.7 \pm 0.4) \times 10^{14}$	$(6.3 \pm 1.2) \times 10^{-25}$
$h \times 203$ MHz	$k_B \times 9.8$ mK	0.22 ± 0.04	$(6.8 \pm 0.5) \times 10^{14}$	$(8.2 \pm 2.0) \times 10^{-25}$
$h \times 246$ MHz	$k_B \times 11.8$ mK	0.31 ± 0.05	$(7.9 \pm 0.6) \times 10^{14}$	$(8.4 \pm 1.9) \times 10^{-25}$
$h \times 290$ MHz	$k_B \times 13.9$ mK	0.35 ± 0.09	$(8.9 \pm 0.7) \times 10^{14}$	$(7.7 \pm 2.3) \times 10^{-25}$

Table 6.1: Three-body loss rates from experiment, γ_3 , with corresponding density and three-body loss event rate constant, K_3^{exp} , according to FORT potential depth in terms of both temperature and frequency values.

for the stable thermal density profile in conjunction with the measured values for the three-atom loss rate, γ_3 , experimental values for the three-body recombination event rate constant, K_3^{exp} were computed as shown in Table 6.1. Because the K_3^{exp} values

show clear agreement with overlapping uncertainty ranges independent of density, a mean is determined, $\bar{K}_3^{exp} = (7.65 \pm 0.47) \times 10^{-25} \text{ cm}^6/\text{sec}$.

6.2 Two-Body Dynamics

Similar to relation for K_3^{exp} in Eq. 6.1, experimental values for the two-body loss event rate constant, K_2^{exp} , were calculated using,

$$\gamma_2 = K_2^{exp} \int_{\text{All space}} n^2(\mathbf{r}) dr^2 \quad (6.4)$$

where the atomic density, $n(\mathbf{r})$ is instead normalized to $N = 2$. The values of K_2^{exp} are listed alongside the experimental rate constants, γ_2 and γ_3 in Table 6.2. The plots in Figs. 6.1 combined with the results in Table 6.2 indicate that the mechanism responsible for two-body trap loss quickly becomes more significant than that of three-body loss when the depth of the FORT is increased. Furthermore, Table 6.2 shows that K_2^{exp} is density-dependent. The reason for this two-body loss most likely

Trap Depth		γ_3 (1/sec)	γ_2 (1/sec)	K_2^{exp} (cm ⁻³ /sec)
(Frequency)	(Temperature)			
$h \times 160 \text{ MHz}$	$k_B \times 7.7 \text{ mK}$	0.12 ± 0.01	0.09 ± 0.01	$(1.5 \pm 0.1) \times 10^{-25}$
$h \times 203 \text{ MHz}$	$k_B \times 9.8 \text{ mK}$	0.22 ± 0.04	0.32 ± 0.02	$(4.4 \pm 0.4) \times 10^{-25}$
$h \times 246 \text{ MHz}$	$k_B \times 11.8 \text{ mK}$	0.31 ± 0.05	0.51 ± 0.02	$(6.1 \pm 0.5) \times 10^{-25}$
$h \times 290 \text{ MHz}$	$k_B \times 13.9 \text{ mK}$	0.35 ± 0.09	0.85 ± 0.04	$(9.5 \pm 0.7) \times 10^{-25}$

Table 6.2: Comparison of three-body loss rates from experiment, γ_3 , to two-body loss rates, γ_2 , and two-body loss event rate constant, K_2^{exp} , according to FORT potential depth in terms of both frequency and potential values.

owes to gained energy in a photoassociative process [74]. As illustrated in Fig. 6.2, when light with a frequency near-resonant to the molecular state transition is present, the two colliding atoms may undergo a transfer to the upper potential curve. The two states can couple only when their energies are degenerate. The atoms enter on the lower curve in Fig. 6.2 with relatively low kinetic energy. Though after transferring to some off-resonant point on the upper curve, depending on the lifetime of the molecular state as well as the laser intensity, the atoms 'roll' down that potential curve gaining energy, then spontaneously emit a photon resulting in trap loss. If the laser intensity is increased, the off-resonant coupling of the transition becomes stronger

up to some saturation level, which allows the transition to happen even when the frequency of the light is far from resonant. This effect is known as power broadening of spectral lines. Additionally, the excited molecule then picks up a higher probability to relax via stimulated emission possibly to a cold molecule [74].

Passagem et. al. showed that coupling transitions to higher molecular vibrational states exist in the vicinity of 1064 nm (FORT beam wavelength) [75]. Importantly, the intensity of the photoassociative light used in that experiment is lower than in this experimental scenario by factors of 3 to 6 for the listed experimental FORT depths. Therefore, it seems that with a higher intensity of FORT light, the off-resonant coupling to higher energy molecular states becomes stronger, resulting in a shorter excited state lifetime and faster two-atom loss from the trap. This follows the observed trend in rate increase but warrants further future investigation into the plausibly complex interaction dynamics.

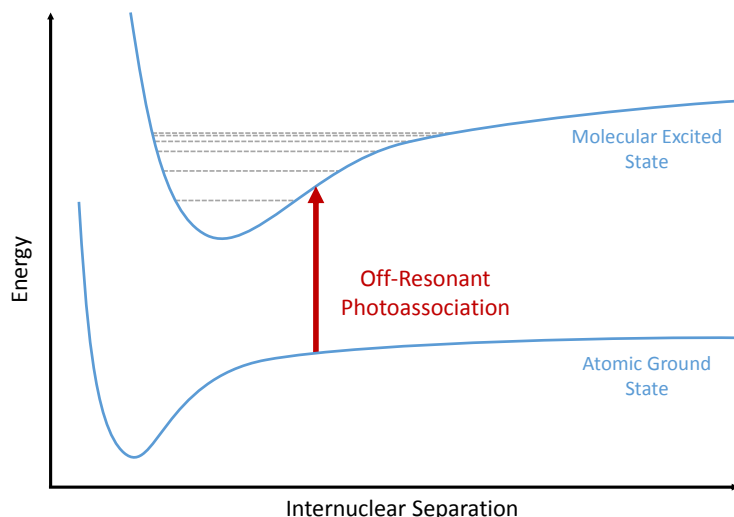


Figure 6.2: A general schematic representation photoassociation due to off-resonant coupling light. Atoms undergoing a collision following the lower **blue** curve can transition to the upper molecular state **blue** curve even if the energy of the incident light (**red arrow**) does not exactly correspond to a molecular bound state (**gray dotted lines**).

6.3 Discussion of Results

The mean value extracted from experimental data for the three-body recombination event rate constant, $\bar{K}_3^{exp} = (7.65 \pm 0.47) \times 10^{-25} \text{ cm}^6/\text{sec}$, is taken to be the main result of this thesis. It exhibits a relative uncertainty of 6.1%. Recall that

the value calculated from established theory using other experimentally determined parameters in [61], was $K_3^{th} = (7.47 \pm 0.51) \times 10^{-25} \text{ cm}^6/\text{sec}$ (see Sec. 3.2.4), which carries 6.8% relative uncertainty.

The mean values of experimental and theoretical K_3 are very close with a discrepancy of 2.4%, i.e.

$$\Delta K_3 = \frac{|\bar{K}_3^{exp} - K_3^{th}|}{K_3^{th}} = 0.024 \quad (6.5)$$

The discrepancy relative to the deviations of the means may also be considered,

$$(\Delta K_3)_{rel} = \frac{|\bar{K}_3^{exp} - K_3^{th}|}{\sqrt{(\delta \bar{K}_3^{exp})^2 + (\delta K_3^{th})^2}} = 0.26 \quad (6.6)$$

Since $(\Delta K_3)_{rel} < 1$, the range of uncertainties is larger than the discrepancy in the mean values. Overall, the experimental and theoretical K_3 quantities show good agreement under consideration of their uncertainties as demonstrated by the low mean discrepancy and large overlap of uncertainty ranges.

Even though the measured value for K_3 corresponds well with the theoretical prediction, there are multiple candidates for systematic error in the experiment. As previously discussed, the averaged temperature determined from release and recapture measurements exhibits a source of experimental variability. In addition, the true characteristics of the FORT beam inside the science chamber cannot truly be known but only estimated. The beam waist, for example, was measured with a microscope and optical imaging system designed to model the beam path into the science chamber, but thus presents another source for potential systematic error. Along with this, the real intensity of the FORT beam, which translates to the potential depth, could only be seen outside of the chamber. Although this serves as the most reasonable estimate to work from, the actual power of the beam is thought to be slightly lower when seen by the atoms due to a slight spatial cropping by the high NA lens. Furthermore, in the analysis of the histograms plotted from SPCM data, the distributions representing the number of atoms in the trap showed substantial overlap as previously discussed. This provided some statistical uncertainty to the final computations. Ultimately, propagating as many factors into the deduction of \bar{K}_3^{exp} as feasibly possible produces a meaningful result as well as a standard to grow from in future few-body experiments in this lab and elsewhere.

In addition to possible systematics, another underlying source of imaginable uncertainty in the analysis of the experimental results is interpretative. Using Eq. 6.1 and 6.4 to obtain the three-body recombination rate constant, K_3^{exp} , and the two-body loss event rate constant, K_2^{exp} , from the experimental atom loss rates, γ_2 and γ_3 , may mix the regimes of *few-body* and *many-body*. These relations are standard in the field of many-body physics, and so were used to calculate results here, but they may not be completely valid for the few-body scenario of the presented experiment. This point is left as an open question to investigate in further work on this project.

6.3.1 Comparison to Results from BEC Experiments

To the extent of my knowledge at the time of submission of this thesis, there have been three experimental investigations into three-body recombination of ^{85}Rb exhibited in references [7, 61, 66]. Each of these measurements of K_3 use the method of loss observation from a large population of ultracold atoms, which ultimately presents the main technical challenge of discerning contributions to the loss signal from two- and three- body processes. Note that K_3 needs to be multiplied by a factor of 3! when translating between condensed and thermal, or noncondensed, atoms [76]. A clear result comes from Roberts et. al., who determined the atom-loss rate constant $K_3 = 4.24_{-0.29}^{+0.70} \pm 0.85 \times 10^{-25} \text{ cm}^6/\text{sec}$ for thermal atoms with an applied magnetic field of 250 G (corresponds to $a = -387a_0 \pm 3a_0$ using Eq. 3.38) [7]. To compare the three-atom loss *event* rate constant, a factor of 1/3 need be included to signify that three atoms are lost per event. Therefore, their analogous result is actually $K_3 = 1.41_{-0.10}^{+0.23} \pm 0.28 \times 10^{-25} \text{ cm}^6/\text{sec}$. This serves as an interesting analog to the measurement presented in this thesis, as it is close to equal distance in terms of scattering length, a , from the Feschbach resonance position at 155 G where $a \rightarrow \infty$. For consideration, if those experimental parameters are used in the same model as utilized here, see Eq. 3.37, a theoretically predicted value of $K_3^{th} = (1.74 \pm 0.11) \times 10^{-25} \text{ cm}^6/\text{sec}$ results. The mean values in that case exhibit a discrepancy of 20%. The larger difference from theory in this case is most likely due to the approximate methods used to describe BEC dynamics rather than in the direct observation method as discussed in Sec. 3.3.

7 | Conclusion

There is certainly no shortage of questions to answer in atomic physics theoretically and experimentally. In actuality, it is when the two work in unison that established ideas gain clarity and new concepts come to light. Through the work in this thesis, novel experimental techniques have been utilized to portray established theory with additional transparency and relative simplicity. The presented observation and measurement of few-body dynamics on the single atom level serves as another step in the perpetual pursuit of understanding in the quantum regime.

To begin, a conceptual understanding of the methods of laser cooling and trapping were introduced followed by a discussion of two-atom collisions. The collision ideas were then extended into a three-atom situation. Here, it was found that the short-range characteristics of the interaction potential along with universal properties of these interactions dictate the behavior of a three-atom scattering process overall. Moreover, it is actually the two-atom property of scattering length, a , that tunes the process of interest - three-body recombination. When three atoms with a negative scattering length collide, there exists a condition in which two of them form a deeply bound state and the third is left free. Because of the excess energy introduced in the binding process, all three atoms can potentially gain enough energy to leave a reasonably deep potential well. The rate constant of recombination, K_3 , depends most notably on a^4 .

Rather than discerning the recombination process as partial trap loss from a cloud of atoms in a BEC state, an experiment that directly measured three-atom inelastic collisions was presented. Single atoms were isolated in a FORT via repulsive light-assisted collisions using a MOT cloud as a starting point. Then by implementing a control system over three separate atoms in independent FORTs, their interaction in one potential well could be managed. Merging three microtraps required the employment of a dynamic and stable AOM system to near-adiabatically combine the atoms. After setting a merged potential depth and interaction duration, time

dependent trap loss was measured. The loss occurred in varieties of one-, two-, and three- body mechanisms, and each was fit into a system of linear decay curves. Extracting the three-body loss rate constant and computing the three-atom density then lead to a readily available experimental value for K_3 . The reasonably simple experimental measurement of K_3 ultimately showed significant agreement with the same value predicted in theory demonstrating a promising avenue for future few-body experimental studies.

With the work presented in this thesis, I have introduced a promising tool for improved three-atom studies. By adapting a unique experimental system from single to few-body operation, the first observation of three-atom recombination events in individually assembled triads was achieved. In addition, an interesting trend of two-body loss enhanced by larger trap depths was observed.

Future Work

Local to this research group, further work may first focus on tightening the precision of these experimental methods. Although there is perhaps always room for better precision of measurement, a potential range of systematic uncertainty ultimately played a significant role in this experiment. Minimizing the inherent uncertainties in the apparatus will likely require adaptation of methods in this case. For example, the release and recapture technique used to measure atomic temperature could be replaced by more accurate comparison of sidebands in Raman spectroscopy [73].

Furthermore, an investigation into the validity of the comparison between loss rates in this *few-body* experiment and results from *many-body* theory will ultimately strengthen the conclusions of this thesis. Namely, the deduction of K_3 from the experimentally determined γ_3 using a thermal density profile for three atoms may not actually be sufficient to transfer between the few-body measurement (γ_3) and many-body observable (K_3). Since the use of Eqs. 6.1 and 6.4 is a standard method in the relevant literature, the calculations were carried out in this form throughout this thesis. However, the ready comparison between few-body and many-body physics in this way raises interesting questions of analysis warranting further study – for example, how does one accurately model the density profile of a three-atom sample?

Cooling of the three atoms to their vibrational ground state using Raman sideband cooling would also be an interesting extension of this project. Not only would collision dynamics become more exaggerated, but an investigation into more complicated molecular formation mechanisms could ensue. Even the first observation of a

^{85}Rb trimer molecule would become plausible. The fundamentals of photoassociative molecular formation are currently of great interest in the field, and a controllable system of three atoms in their ground state could provide an unprecedented level of precision [77].

One could view this project not only as a finer scale view of ultracold atom dynamics, but also, in a sense, as one piece of a base layer in the long term goal of deterministically building molecules atom-by-atom. With ever improving knowledge and control of the transition from atoms to molecules it indeed seems feasible to follow the thoughts of Richard Feynman [78],

"But it is interesting that it would be, in principle, possible (I think) for a physicist to synthesize any chemical substance that the chemist writes down. Give the orders and the physicist synthesizes it. How? Put the atoms down where the chemist says, and so you make the substance. The problems of chemistry and biology can be greatly helped if our ability to see what we are doing, and to do things on an atomic level, is ultimately developed – a development which I think cannot be avoided."

A | Direct Atom Triad Loss Model Solutions

In Section 3.3.2, the system of loss-rate equations that describes the evolution of the trap loss parameters was defined.

$$\dot{N}_3(t) = -\gamma_3 N_3 - \gamma_2(3N_3) - \gamma_1(3N_3) \quad (\text{A.1a})$$

$$\dot{N}_2(t) = -\gamma_2 N_2 - \gamma_1(2N_2) + \gamma_1(3N_3) \quad (\text{A.1b})$$

$$\dot{N}_1(t) = -\gamma_1 N_1 + \gamma_2(3N_3) + \gamma_1(2N_2) \quad (\text{A.1c})$$

$$\dot{N}_0(t) = \gamma_3 N_3 + \gamma_2 N_2 + \gamma_1 N_1 \quad (\text{A.1d})$$

The solutions to this system are then used to fit the data collected by the SPCM discussed in Section 6.1. To solve the set of equations, first begin with Eq. A.1a, which is linear in N_3 ,

$$\dot{N}_3(t) = -(\gamma_3 + 3\gamma_2 + 3\gamma_1)N_3 \quad (\text{A.2})$$

Since it is separable, the standard solution is found to be,

$$N_3(t) = A \exp[-(\gamma_3 + 3\gamma_2 + 3\gamma_1)t] \quad (\text{A.3})$$

where A is a constant of integration determined from initial conditions, or more specifically percentage of 3-atom counts in the total population at $t = 0$.

The solution in Eq. A.3 can then be substituted into Eq. A.1b,

$$\dot{N}_2(t) + (\gamma_2 + 2\gamma_1)N_2 = 3A\gamma_1 \exp[-(\gamma_3 + 3\gamma_2 + 3\gamma_1)t] \quad (\text{A.4})$$

Multiplying each side of this equation by an integrating factor, $\exp[\int(\gamma_2 + 2\gamma_1)dt] =$

$\exp[(\gamma_2 + 2\gamma_1)t]$, and integrating yields the solution for N_2 ,

$$N_2(t) = \frac{-3A\gamma_1}{\gamma_3 + \gamma_2 + \gamma_1} \exp[-(\gamma_3 + 3\gamma_2 + 3\gamma_1)t] + B \exp[-(\gamma_2 + 2\gamma_1)t] \quad (\text{A.5})$$

where B is again a constant of integration found from the initial ($t = 0$) percentage of the population measured to be two atoms.

Now, Eq. A.1c can be substituted and simplified to be linear as well,

$$\begin{aligned} \dot{N}_1(t) + \gamma_1 N_1 &= \left(3A\gamma_2 - \frac{6A\gamma_1^2}{\gamma_3 + \gamma_2 + \gamma_1} \right) \exp[-(\gamma_3 + 3\gamma_2 + 3\gamma_1)t] \\ &\quad + 2B\gamma_1 \exp[-(\gamma_2 + 2\gamma_1)t] \end{aligned} \quad (\text{A.6})$$

Again, multiplying each side by an integrating factor, $\exp(\int \gamma_1 dt) = \exp(\gamma_1 t)$ and integrating yields the solution,

$$N_1(t) = -\alpha \exp[-(\gamma_3 + 3\gamma_2 + 3\gamma_1)t] - \beta \exp[-(\gamma_2 + 2\gamma_1)t] + C \exp(-\gamma_1 t) \quad (\text{A.7})$$

where,

$$\begin{aligned} \alpha &= \left(\frac{3A}{\gamma_3 + 3\gamma_2 + 2\gamma_1} \right) \left[\gamma_2 - \left(\frac{2\gamma_1^2}{\gamma_3 + 2\gamma_2 + \gamma_1} \right) \right] \\ \beta &= \left(\frac{2B\gamma_1}{\gamma_2 + \gamma_1} \right) \end{aligned} \quad (\text{A.8})$$

and C is a constant of integration defined from the initial percentage of the population measured to be one atom.

Finally, each of these solutions can be inserted into Eq. A.1d,

$$\begin{aligned} \dot{N}_0(t) &= \left(A\gamma_3 - \frac{3A\gamma_1\gamma_2}{\gamma_3 + \gamma_2 + \gamma_1} - \alpha\gamma_1 \right) \exp[-(\gamma_3 + 3\gamma_2 + 3\gamma_1)t] \\ &\quad + (B\gamma_2 - \beta\gamma_1) \exp[-(\gamma_2 + 2\gamma_1)t] + C\gamma_1 \exp(-\gamma_1 t) \end{aligned} \quad (\text{A.9})$$

This equation is autonomous, so it is readily integrated to find the solution,

$$\begin{aligned} N_0(t) = & \left[-\gamma_3 A + \left(\frac{3A\gamma_1\gamma_2}{\gamma_3 + 2\gamma_2 + \gamma_1} \right) + \gamma_1 \alpha \right] \left(\frac{1}{\gamma_3 + 3\gamma_2 + 3\gamma_1} \right) \exp[-(\gamma_3 + 3\gamma_2 + 3\gamma_1)t] \\ & + (-\gamma_2 B + \gamma_1 \beta) \left(\frac{1}{\gamma_2 + 2\gamma_1} \right) \exp[-(\gamma_2 + 2\gamma_1)t] - C \exp(-\gamma_1 t) + D \end{aligned} \quad (\text{A.10})$$

where D is a constant of integration defined from the percentage of 'zero' atom counts at $t = 0$.

After combining all fluorescence data collected in the SPCM when 'Wait Time' = $t = 0$, the initial populations of one, two, and three atoms in the trap were found to be,

$$N_3(0) = 0.836, \quad N_2(0) = 0.022, \quad N_1(0) = 0.141, \quad N_0(0) = 0.002 \quad (\text{A.11})$$

Bibliography

- [1] S. N. Bose. Plancks gesetz und lichtquantenhypothese. *Zeitschrift für Physik*, 26:178–181, 1924.
- [2] A. Griffin, D. W. Snoke, and S. Stringari, editors. *Bose-Einstein Condensation*. Cambridge University Press, 1995.
- [3] M. H. Anderson, J. R. Ensher, M. R. Matthews, C. E. Wieman, and E. A. Cornell. Observation of Bose-Einstein condensation in a dilute atomic vapor. *Science*, 269(5221):198–201, 1995.
- [4] S. L. Cornish, S. T. Thompson, and C. E. Wieman. Formation of bright matter-wave solitons during the collapse of attractive Bose-Einstein condensates. *Phys. Rev. Lett.*, 96(17):170401, 2006.
- [5] M. Ueda and A. J. Leggett. Macroscopic quantum tunneling of a Bose-Einstein condensate with attractive interaction. *Phys. Rev. Lett.*, 80(8):1576–1579, 1998.
- [6] E. A. Donley, N. R. Claussen, S. L. Cornish, J. L. Roberts, E. A. Cornell, and C. E. Wieman. Dynamics of collapsing and exploding Bose-Einstein condensates. *Nature*, 412:295, 2001.
- [7] J. L. Roberts, N. R. Claussen, S. L. Cornish, and C. E. Wieman. Magnetic field dependence of ultracold inelastic collisions near a Feshbach resonance. *Phys. Rev. Lett.*, 85(4):728–731, 2000.
- [8] J. Söding, D. Guéry-Odelin, P. Desbiolles, F. Chevy, H. Inamori, and J. Dalibard. Three-body decay of a rubidium Bose-Einstein condensate. *App. Phys. B*, 69(4):257–261, 1999.
- [9] B. D. Esry, C. D. Lin, and C. H. Greene. Adiabatic hyperspherical study of the helium trimer. *Phys. Rev. A*, 54(1):394–401, 1996.
- [10] E. Braaten and H.-W. Hammer. Three-body recombination into deep bound states in a Bose gas with large scattering length. *Phys. Rev. Lett.*, 87(160407), 2001.
- [11] W. Neuhauser, M. Hohenstatt, P. E. Toschek, and H. Dehmelt. Localized visible Ba⁺ mono-ion oscillator. *Phys. Rev. A*, 22(3):1137–1140, 1980.
- [12] Z. Hu and H. J. Kimble. Observation of a single atom in a magneto-optical trap. *Opt. Lett.*, 19(22):1888–1890, 1994.
- [13] W. S. Bakr, A. Peng, M. E. Tai, R. Ma, J. Simon, J. I. Gillen, S. Foelling, L. Pollet,

and M. Greiner. Probing the superfluid to Mott insulator transition at the single atom level. *Science*, 329(5991):547–550, 2010.

- [14] A. Itah, H. Veksler, O. Lahav, A. Blumkin, C. Moreno, C. Gordon, and J. Steinhauer. Direct observation of a sub-Poissonian number distribution of atoms in an optical lattice. *Phys. Rev. Lett.*, 104(11):113001, 2010.
- [15] J. F. Sherson, C. Weitenberg, M. Endres, M. Cheneau, I. Bloch, and S. Kuhr. Single-atom resolved fluorescence imaging of an atomic mott insulator.
- [16] A. G. Manning, R. Khakimov, R. G. Dall, and A. G. Truscott. Single-atom source in the picokelvin regime. *Phys. Rev. Lett.*, 113(13):130403, 2014.
- [17] R. Grimm, M. Weidemüller, and Y. B. Ovchinnikov. Optical dipole traps for neutral atoms. *Advances in Atomic, Molecular and Optical Physics*, 42:95–170, 1999.
- [18] N. Schlosser, G. Reymond, I. Protsenko, and P. Grangier. Sub-Poissonian loading of single atoms in a microscopic dipole trap. *Nature*, 411:1024, 2001.
- [19] N. Schlosser, G. Reymond, and P. Grangier. Collisional blockade in microscopic optical dipole traps. *Phys. Rev. Lett.*, 89(2):023005, June 2002.
- [20] T. Grünzweig, A. Hilliard, M. McGovern, and M. F. Andersen. Near-deterministic preparation of a single atom in an optical microtrap. *Nature Physics*, 6:951, 2010.
- [21] A. V. Carpentier, Y. H. Fung, P. Sompet, A. J. Hilliard, T. G. Walker, and M. F. Andersen. Preparation of a single atom in an optical microtrap. *Laser Physics Letters*, 10(12):125501, 2013.
- [22] D. H. McIntyre, C. A. Manogue, and J. Tate. *Quantum Mechanics: A Paradigm Approach*. Pearson Boston, 2012.
- [23] D. A. Steck. Rubidium 85 D line data. <http://steck.us/alkalidata> (revision 2.1.6, 2013), 2013.
- [24] A. L. Migdall, J. V. Prodan, W. D. Phillips, T. H. Bergeman, and H. J. Metcalf. First observation of magnetically trapped neutral atoms. *Phys. Rev. Lett.*, 54(24):2596–2599, 1985.
- [25] P. D. Lett, R. N. Watts, C. I. Westbrook, W. D. Phillips, P. L. Gould, and H. J. Metcalf. Observation of atoms laser cooled below the Doppler limit. *Physical Rev. Lett.*, 61(2):169, 1988.
- [26] D. S. Weiss, E. Riis, Y. Shevy, P. J. Ungar, and S. Chu. Optical molasses and multilevel atoms: experiment. *JOSA B*, 6(11):2072–2083, 1989.
- [27] J. Dalibard and C. Cohen-Tannoudji. Laser cooling below the doppler limit by polarization gradients: simple theoretical models. *J. Opt. Soc. Am. B*, 6(11):2023–2045, 1989.
- [28] D. J. Wineland, J. Dalibard, and C. Cohen-Tannoudji. Sisyphus cooling of a bound atom. *J. Opt. Soc. Am. B*, 9(1):32–42, 1992.

- [29] J. Dalibard and C. Cohen-Tannoudji. Dressed-atom approach to atomic motion in laser light: the dipole force revisited. *J. Opt. Soc. Am. B*, 2(11):1707–1720, 1985.
- [30] J. Weiner. *Cold and ultracold collisions in quantum microscopic and mesoscopic systems*. Cambridge University Press, 2003.
- [31] V. S. Letokhov. Doppler line narrowing in a standing light wave. *JETP Lett.*, 7:272, 1968.
- [32] S. Chu, J. E. Bjorkholm, A. Ashkin, and A. Cable. Experimental observation of optically trapped atoms. *Phys. Rev. Lett.*, 57(3):314, 1986.
- [33] J. D. Jackson. *Classical Electrodynamics*. Wiley, 1999.
- [34] C. Cohen-Tannoudji, J. Dupont-Roc, and G. Grynberg. The dressed atom approach. *Atom-Photon Interactions: Basic Process and Applications*, pages 407–514, 2008.
- [35] B. H. Bransden and C. J. Joachain. *Physics of Atoms and Molecules (2nd Edition)*. Pearson, 2003.
- [36] Y. H. Fung and M. F. Andersen. Efficient collisional blockade loading of a single atom into a tight microtrap. *New Journal of Physics*, 17(7):073011, 2015.
- [37] P. R. Fontana. Theory of long-range interatomic forces. i. dispersion energies between unexcited atoms. *Phys. Rev.*, 123(5):1865–1870, 1961.
- [38] T. Grünzweig, M. McGovern, A. J. Hilliard, and M. F. Andersen. Using light-assisted collisions to consistently isolate individual atoms for quantum information processing. *Quantum Information Processing*, 10(6):925, 2011.
- [39] C. Zener. Non-adiabatic crossing of energy levels. *Proceedings of the Royal Society of London. Series A, Containing Papers of a Mathematical and Physical Character*, 137(833):696–702, 1932.
- [40] P. S. Julienne. Cold binary atomic collisions in a light field. *Journal of Research of the National Institute of Standards and Technology*, 101(4):487–503, 1996.
- [41] M. Lyon and S. L. Rolston. Ultracold neutral plasmas. *Reports on Progress in Physics*, 80(1):017001, 2016.
- [42] D. L. Baulch, C. J. Cobos, R. A. Cox, C. Esser, P. Frank, T. H. Just, J. A. Kerr, M. J. Pilling, J. Troe, R. W. Walker, et al. Evaluated kinetic data for combustion modelling. *Journal of Physical and Chemical Reference Data*, 21(3):411–734, 1992.
- [43] R. C. Forrey. Rate of formation of hydrogen molecules by three-body recombination during primordial star formation. *Astrophysical Journal Letters*, 773(2):L25, 2013.
- [44] L. D. Landau and E. M. Lifshitz. *Quantum Mechanics*, volume 3. Pergamon Press Ltd., 1958.
- [45] L. D. Fadeev. Scattering theory for a three-particle system. *Sov. Phys. JETP*,

12(5), 1961.

- [46] E. O. Alt, P. Grassberger, and W. Sandhas. Reduction of the three-particle collision problem to multi-channel two-particle Lippmann-Schwinger equations. *Nuc. Phys. B*, 2(2):167–180, 1967.
- [47] L. M. Delves. Tertiary and general-order collisions. *Nuc. Phys.*, 9(3):391–399, 1958.
- [48] L. M. Delves. Tertiary and general-order collisions (ii). *Nuc. Phys.*, 20:275–308, 1960.
- [49] Y. Wang, J. P. D’Incao, and B. D. Esry. Ultracold few-body systems. In Ennio Arimondo, Paul R. Berman, and Chun C. Lin, editors, *Advances in Atomic, Molecular, and Optical Physics*, volume 62, chapter 1, pages 1–115. Elsevier Inc., 2013.
- [50] R. C. Whitten and F. T. Smith. Symmetric representation for three-body problems. ii. motion in space. *Journal of Mathematical Physics*, 9(7):1103–1113, 1968.
- [51] A. Kuppermann. Reactive scattering with row-orthonormal hyperspherical coordinates. 1. transformation properties and hamiltonian for triatomic systems. *J. Phys. Chem.*, 100(7):2621–2636, 1996.
- [52] J. P. D’Incao, F. Anis, and B. D. Esry. Ultracold three-body recombination in two dimensions. *Phys. Rev. A*, 91(6):062710, 2015.
- [53] O.I. Kartavtsev and A.V. Malykh. Universal low-energy properties of three two-dimensional bosons. *Phys. Rev. A*, 74(4):042506, 2006.
- [54] J. P. D’Incao and B. D. Esry. Adiabatic hyperspherical representation for the three-body problem in two dimensions. *Phys. Rev. A*, 90(4):042707, 2014.
- [55] V. Efimov. Low-energy properties of three resonantly interacting particles. *Sov. J. Nucl. Phys.*, 29(4):546–553, 1979.
- [56] J. Avery. *Hyperspherical Harmonics*. Kluwer Academic Publishers, 1989.
- [57] B. D. Esry, C. H. Greene, and H. Suno. Threshold laws for three-body recombination. *Phys. Rev. A*, 65(1):010705, 2001.
- [58] E. Braaten and H.-W. Hammer. Universality in few-body systems with large scattering length. *Physics Reports*, 428(5):259–390, 2006.
- [59] J. Wang, J. P. D’Incao, B. D. Esry, and C. H. Greene. Origin of the three-body parameter universality in efimov physics. *Phys. Rev. Lett.*, 108(26):263001, 2012.
- [60] V. Efimov. Energy levels arising from resonant two-body forces in a three-body system. *Phys. Lett. B*, 33(8):563–564, 1970.
- [61] R. J. Wild, P. Makotyn, J. M. Pino, E. A. Cornell, and D. S. Jin. Measurements of Tan’s contact in an atomic Bose-Einstein condensate. *Phys. Rev. Lett.*, 108(14):145305, 2012.

- [62] F. Ferlaino, A. Zenesini, M. Berninger, B. Huang, H.-C. Nägerl, and R. Grimm. Efimov resonances in ultracold quantum gases. *Few-Body Systems*, 51(2-4):113, 2011.
- [63] A. J. Moerdijk, B. J. Verhaar, and A. Axelsson. Resonances in ultracold collisions of ^6Li , ^7Li , and ^{23}Na . *Phys. Rev. A*, 51(6):4852–4861, 1995.
- [64] N. R. Claussen, S. J. J. M. F. Kokkelmans, S. T. Thompson, E. A. Donley, E. Hodby, and C. Wieman. Very-high-precision bound-state spectroscopy near a ^{85}Rb Feshbach resonance. *Phys. Rev. A*, 67, 2003.
- [65] J. Stenger, S. Inouye, M. R. Andrews, H.-J. Miesner, D. M. Stamper-Kurn, and W. Ketterle. Strongly enhanced inelastic collisions in a Bose-Einstein condensate near Feshbach resonances. *Physical Rev. Lett.*, 82(12):2422, 1999.
- [66] P. A. Altin, G. R. Dennis, G. D. McDonald, D. Döring, J. E. Debs, J. D. Close, C. M. Savage, and N. P. Robins. Collapse and three-body loss in a ^{85}Rb Bose-Einstein condensate. *Phys. Rev. A*, 84(3):033632, 2011.
- [67] K. B. MacAdam, A. Steinbach, and C. Wieman. A narrow-band tunable diode laser system with grating feedback, and a saturated absorption spectrometer for Cs and Rb. *American Journal of Physics*, 60(12):1098–1111, 1992.
- [68] M. McGovern, A. J. Hilliard, T. Grünzweig, and M. F. Andersen. Counting atoms in a deep optical microtrap. *Opt. Lett.*, 36(7):1041–1043, 2011.
- [69] A. J. Hilliard, Y. H. Fung, P. Sompét, A. V. Carpentier, and M. F. Andersen. In-trap fluorescence detection of atoms in a microscopic dipole trap. *Phys. Rev. A*, 91(5):053414, 2015.
- [70] A. M. Kaufman, B. J. Lester, C. M. Reynolds, M. L. Wall, M. Foss-Feig, K. R. A. Hazzard, A. M. Rey, and C. A. Regal. Two-particle quantum interference in tunnel-coupled optical tweezers. *Science*, 345(6194):306–309, 2014.
- [71] C. Tuchendler, A. M. Lance, A. Browaeys, Y. R. P. Sortais, and P. Grangier. Energy distribution and cooling of a single atom in an optical tweezer. *Phys. Rev. A*, 78(3):033425, 2008.
- [72] C. Kittel and H. Kroemer. *Thermal Physics*. W.H. Freeman and Company, 2nd edition, 1980.
- [73] P. Sompét, Y. H. Fung, E. Schwartz, M. D. J. Hunter, J. Phrompao, and M. F. Andersen. Zeeman-insensitive cooling of a single atom to its two-dimensional motional ground state in tightly focused optical tweezers. *Phys. Rev. A*, 95(3):031403, 2017.
- [74] K. M. Jones, E. Tiesinga, P. D. Lett, and P. S. Julienne. Ultracold photoassociation spectroscopy: Long-range molecules and atomic scattering. *Reviews of Modern Physics*, 78(2):483, 2006.
- [75] H. F. Passagem, R. Colin-Rodriguez, P. C. V. da Silva, N. Bouloufa-Maafa, O. Dulieu, and L. G. Marcassa. Formation of ultracold molecules induced by a high-power single-frequency fiber laser. *J. Phys. B*, 50(4):045202, 2017.

- [76] E. A. Burt, R. W. Ghrist, C. J. Myatt, M. J. Holland, E. A. Cornell, and C. E. Wieman. Coherence, correlations, and collisions: What one learns about Bose-Einstein condensates from their decay. *Phys. Rev. Lett.*, 79:337, 1997.
- [77] L. R. Liu, J. D. Hood, Y. Yu, J. T. Zhang, N. R. Hutzler, T. Rosenband, and K.-K. Ni. Building one molecule from a reservoir of two atoms. *Science*, 360(6391):900–903, 2018.
- [78] R. Feynman. There’s plenty of room at the bottom. *Caltech Engineering and Science*, 23:5:22–36, 1960.